J. Fluid Mech. (2004), *vol.* 508, *pp.* 333–371.
DOI: 10.1017/S0022112004009346 Printed in the United Kingdom

Exact coherent structures in pipe flow: travelling wave solutions

By H. WEDIN AND R. R. KERSWELL†

Department of Mathematics, University of Bristol, Bristol, BS8 1TW, UK

(Received 30 October 2003 and in revised form 13 February 2004)

Three-dimensional travelling wave solutions are found for pressure-driven fluid flow through a circular pipe. They consist of three well-defined flow features – streamwise rolls and streaks which dominate and streamwise-dependent wavy structures. The travelling waves can be classified by the m-fold rotational symmetry they possess about the pipe axis with $m = 1$, 2, 3, 4, 5 and 6 solutions identified. All are born out of saddle-node bifurcations with the lowest corresponding to $m = 3$ and traceable down to a Reynolds number (based on the mean velocity) of 1251. The new solutions are found using a constructive continuation procedure based upon key physical mechanisms thought generic to wall-bounded shear flows. It is believed that the appearance of these new alternative solutions to the governing equations as the Reynolds number is increased is a necessary precursor to the turbulent transition observed in experiments.

1. Introduction

The stability of pressure-driven flow through a long circular pipe is one of the most classical and intriguing problems in fluid mechanics. Ever since the original experiments of Reynolds (1883), it has been known that the steady, unidirectional Hagen–Poiseuille flow, uniquely realized at low Reynolds numbers Re, can undergo transition to turbulence when disturbed sufficiently strongly at high enough Reynolds numbers. Subsequent experimental work has confirmed and extended Reynolds's first observations to study how transition occurs and the subsequent possibly intermittent turbulent state (Wygnanski & Champagne 1973; Wygnanski, Sokolov & Friedman 1975; Darbyshire & Mullin 1995; Draad, Kuiken & Nieuwstadt 1998; Eliahou, Tumin & Wygnanski 1998; Han, Tumin & Wygnanski 2000; Hof, Juel & Mullin 2003). What consistently emerges is the sensitivity of the transition onset to the exact form of the perturbation and how the size of the threshold amplitude required to trigger transition decreases with increasing Reynolds number (Darbyshire & Mullin 1995; Hof *et al.* 2003). The fact that this unidirectional flow is believed linearly stable (Lessen, Sadler & Liu 1968; Garg & Rouleau 1972; Salwen, Cotten & Grosch 1980; Herron 1991; Meseguer & Trefethen 2003) has served only to highlight the essentially nonlinear origin of the observed transition. Pipe flow is then just one of a class of wall-bounded shear flows which suffer turbulent transition through a process or processes unrelated to the local stability properties of the low-Reynolds-number basic solution. Further examples include plane Couette flow where the basic solution has been proved linearly stable (Romanov 1973) as well as plane Poiseuille flow where the base flow loses stability at a far higher Reynolds number ($Re = 5772$) than that at

† Author to whom correspondence should be addressed: R.R.Kerswell@bris.ac.uk

which transition is observed ($Re \approx 2100$, Rozhdestvensky & Simakin 1984; $Re \approx 2300$, Keefe, Moin & Kim 1992; or using a Reynolds number based on the centreline velocity ≈ 1000, Carlson, Widnall & Peeters 1982).

Recent thinking now views transition in these systems as being an issue revolving around the existence of other solutions that do not have any connection with the basic flow, and their basins of attraction. Pipe flow can be considered as a nonlinear dynamical system $\mathrm{d}\boldsymbol{u}/\mathrm{d}t = \boldsymbol{f}(\boldsymbol{u}; Re)$ defined by the governing Navier–Stokes equations together with the appropriate pressure-gradient forcing and boundary conditions, and Re parametrizing the system. Within this framework, there is one linearly stable fixed point (Hagen–Poiseuille flow) for all Re which is a global attractor for $Re < Re_g$ (nonlinearly stable) but only a local attractor for $Re > Re_g$ (nonlinearly unstable but still linearly stable). It is known that all disturbances to this basic state must decay exponentially if $Re < Re_e = 81.49$ (Joseph & Carmi 1969), the energy stability limit, whereas for $Re_e \leqslant Re < Re_g$, some disturbances can transiently grow but then decay (Boberg & Brosa 1988; Bergström 1993; Schmid & Henningson 1994; O'Sullivan & Breuer 1994; Zikanov 1996). At $Re = Re_g$, new limit sets in phase space (typically steady or periodic solutions to the Navier–Stokes equations) are now presumed born which support the complex dynamics observed at transition. These new solutions are imagined as providing the skeleton about which complicated time-dependent orbits observed in transition may drape themselves so that they no longer evolve back to Hagen–Poiseuille flow at long times (Schmiegel & Eckhardt 1997; Eckhardt *et al.* 2002). As a result, the emergence of these alternative solutions is believed to have a strong relation with the observed lower limit where turbulence is sustainable of $Re_t \approx 1800$–2000 and their existence to structure the transition process itself. The fact that the basic steady solution remains a local attractor in phase space is largely secondary to the fact that its basin of attraction diminishes rapidly as Re increases. This, taken with the fact that the basin boundary is undoubtedly complicated in such a high-dimensional phase space, explains why the (laminar) Hagen–Poiseuille solution is so sensitive to the size and form of an initial disturbance.

The existence of alternative solutions to the Navier–Stokes equations has now been demonstrated in a number of different wall-bounded shear flows (and sometimes clearly observed, e.g. Anson, Mullin & Cliffe 1989). Steady solutions have been found in plane Couette flow down to $Re = 125$ (Nagata 1990; Clever & Busse 1997; or more accurately $Re = 127.7$, Waleffe 2003) compared to a transitional value of $Re \approx 320$–350 (Lundbladh & Johansson 1991; Tillmark & Alfredsson 1992; Daviaud, Hegseth & Bergé 1992; Dauchot & Daviaud 1995; Bottin *et al.* 1998), and travelling wave solutions in plane Poiseuille flow at $Re = 977$ (Waleffe 2003) compared to a transitional value of $Re \approx 2100$–2300 (Rozhdestvensky & Simakin 1984; Keefe *et al.* 1992). What is striking is how the key structural features of these solutions – strong downstream vortices and streaks – coincide with what are observed in experiments as transient coherent structures. The clear implication seems to be that these solutions are saddles in phase space so that the flow dynamics can reside temporarily in their vicinity (the flow approaches near to these solutions in phase space via the stable manifold before being flung away in the direction of the unstable manifold). Given this success, there has been a concerted effort to theoretically find solutions other than the Hagen–Poiseuille state in pipe flow. Despite some suggestive asymptotic analyses (Davey & Nguyen 1971; Smith & Bodonyi 1982; Walton 2002), no non-trivial solutions have so far been reported (Patera & Orszag 1981; Landman 1990*a*, *b*).

The standard approach to finding such nonlinear solutions is homotopy which was used by Nagata (1990) to find the first disconnected solutions in plane Couette flow.

This continuation approach relies on the presence of a neighbouring problem in which nonlinear solutions are known and being able to smoothly continue these solutions back to the original system of interest. Since generally there is no way of knowing whether such a connection exists *a priori*, the approach can be rather hit-and-miss depending more on luck than physical insight. Nevertheless, considerable success has been achieved in the past, building solution 'bridges' between Bénard convection, Taylor–Couette flow, plane Couette flow and plane Poiseuille flow (Nagata 1990, 1997, 1998; Clever & Busse 1992, 1997; Faisst & Eckhardt 2000; Waleffe 2001, 2003). However, no continuation strategy back to pipe flow from another physical system has yet succeeded. Efforts to repeat Nagata's success by trying to continue solutions known in rotating pipe flow (Toplosky & Akylas 1988) back to non-rotating pipe flow have failed (Barnes & Kerswell 2000), and an attempt to use a geometrical embedding of (circular) pipe flow in elliptical pipe flow proved impractical (Kerswell & Davey 1996).

Recently, Waleffe (1998, 2003) has developed a homotopy approach for finding nonlinear solutions to wall-bounded shear flows with clear mechanistic underpinnings. By adding a carefully chosen artificial body force to plane Couette and plane Poiseuille flow, he was able to generate a nearby bifurcation point in the augmented system from which a new solution branch could be smoothly traced back to the original zero-force flow situation. The key steps are selecting the form of the body force and choosing the bifurcation point from which to start the branch continuation. The ideas behind this design process (Waleffe 1995*a*, *b*, 1997) were developed along with coworkers (Hamilton, Kim & Waleffe 1995; Waleffe & Kim 1997, 1998) while trying to understand how turbulence is maintained rather than initiated at low Reynolds numbers (Hamilton *et al.* 1995). The continuation approach is based upon simple physical mechanisms which help remove much of the uncertainty surrounding homotopy and can trace their origins to Benney's mean-flow first-harmonic theory (Benney 1984). The central idea is that in wall-bounded shear flows there is a generic mechanism, christened the 'self-sustaining process' (SSP) by Waleffe, which can lead to solutions with three well-defined flow components – streamwise rolls, streaks and wavelike disturbances – maintaining each other against viscous decay. In isolation, streamwise rolls would secularly decay because of viscosity but, crucially, the presence of other flow structures naturally generated by rolls near a wall can provide just the required energy input to sustain them. The streamwise rolls advect the mean shear alternately to and from the wall (in a spanwise sense) hence lifting slower moving fluid into regions of faster flow and dragging faster flowing fluid into slower flow regions nearer the wall. This produces streaks in the streamwise direction which at certain amplitude and wavelength are linearly unstable through spanwise-inflectional instabilities to axially dependent wave disturbances. Importantly, these wavelike disturbances can drive new streamwise rolls through their nonlinear self-interaction. If the spatial structure of the wavelike disturbances is such that these induced rolls match the initial driving rolls then the initial rolls can be sustained against viscous decay. Waleffe initially explored this idea by cutting open the Navier–Stokes equations and confirming each link of the rolls–streaks–waves cycle piecemeal in the context of plane Couette flow (Waleffe 1997). He then turned the process into a smooth continuation procedure so that the approximately engineered solutions became exact to arbitrary accuracy (Waleffe 1998). Subsequently, the general applicability and success of the approach has been demonstrated in plane Couette and plane Poiseuille flows using either non-slip or stress-free boundary conditions (Waleffe 2001, 2003).

Pipe flow offers an obvious new context in which to test the universality of this approach further which has obvious implications for establishing the generic nature

of transition in wall-bounded shear flows. Also this approach offers a promising new technique to find alternative nonlinear solutions which have proved so enigmatic in this particular problem. As a result the objectives of this paper are twofold: to establish the credentials of this constructive approach and, perhaps only marginally more importantly, to find the solutions themselves.

The plan of the paper is as follows. Section 2 introduces the pipe flow problem, states the governing equations and makes some important definitions. Section 3 discusses the self-sustaining process (SSP) and illustrates how it may be used to find approximate solutions to the governing equations. Although these 'solutions' are not exact since certain terms in the equations are ignored, it appears by appealing to the correct physical mechanisms, that all the important terms have been retained. As a result, each such 'approximate' solution has a high probability of leading to an exact counterpart via a smooth continuation procedure. Section 4 shows how this can be done to arbitrary accuracy using the information gleaned from settling up a SSP 'solution'. Section 5 collects together all the results of the paper before a discussion follows in § 6.

While this work was being completed we became aware that Faisst & Eckhardt (2003) had just isolated converged twofold and threefold rotationally symmetric solutions ($\mathscr{R}_2$ and $\mathscr{R}_3$ waves as defined in (2.12) below) in pipe flow using a similar continuation approach. Here we confirm these findings, discover new branches of the threefold rotationally symmetric ($\mathscr{R}_3$) waves and present converged onefold, fourfold, fivefold and sixfold rotationally symmetric ($\mathscr{R}_1$, $\mathscr{R}_4$, $\mathscr{R}_5$ and $\mathscr{R}_6$) waves solutions for the first time. This paper then complements and extends their study as well as discussing why the continuation approach works.

2. Governing equations

We consider an incompressible fluid of constant density ρ and kinematic viscosity ν flowing in a circular pipe of radius s_0 under the action of a constant applied pressure gradient

$$\nabla p^* = -\frac{4\rho\nu W}{s_0^2}\widehat{z}. \tag{2.1}$$

At low enough values of the Reynolds number $Re := s_0 W/\nu$, the realized flow is uniquely Hagen–Poiseuille flow (HPF)

$$\boldsymbol{u}^* = W\left(1 - \frac{s^2}{s_0^2}\right)\widehat{z}, \tag{2.2}$$

in the usual cylindrical polar coordinate system (s, ϕ, z). The governing equations (non-dimensionalized using the Hagen–Poiseuille centreline speed W and pipe radius s_0) for pipe flow are

$$\frac{\partial \boldsymbol{u}}{\partial t} + \boldsymbol{u}\cdot\nabla\boldsymbol{u} + \nabla p = \frac{1}{Re}\nabla^2\boldsymbol{u} + \frac{4}{Re}\widehat{z}, \tag{2.3}$$

$$\nabla\cdot\boldsymbol{u} = 0, \tag{2.4}$$

with boundary condition

$$\boldsymbol{u}(1, \phi, z) = \boldsymbol{0} \tag{2.5}$$

where $\boldsymbol{u} = \boldsymbol{u}^*/W$ and p represents the pressure deviation away from the imposed gradient. A *mean* Reynolds number can be defined in terms of the mean speed

$$\overline{W} := \frac{1}{\pi}\int_0^{2\pi} \mathrm{d}\phi \int_0^1 s\,\mathrm{d}s\, \boldsymbol{u}^* \cdot \widehat{\boldsymbol{z}} \tag{2.6}$$

of the fluid down the pipe:

$$Re_m := \frac{2s_0\overline{W}}{\nu} \tag{2.7}$$

and in contrast to the pressure-gradient Reynolds number Re, is not known *a priori*. The extent to which Re_m and Re differ is a useful measure of how far the realized flow solution has deviated from HPF, $\boldsymbol{u} = (1-s^2)\widehat{\boldsymbol{z}}$, where they are identical. The energy dissipation rate per unit mass is

$$D := \frac{1}{\pi Re}\lim_{L\to\infty}\frac{1}{2L}\int_{-L}^{L}\mathrm{d}z\int_0^{2\pi}\mathrm{d}\phi\int_0^1 s\,\mathrm{d}s|\nabla\boldsymbol{u}|^2 = \frac{2Re_m}{Re^2} \tag{2.8}$$

in units of W^3/s_0 and the friction coefficient (Schlichting 1968, equation (5.10)) is defined as

$$\Lambda := \frac{1}{\rho}\frac{\mathrm{d}p}{\mathrm{d}z}\Big/\frac{1}{4s_0}\overline{W}^2 = \frac{64Re}{Re_m^2}. \tag{2.9}$$

Computationally, it is preferable to work with the 'perturbation' velocity away from Hagen–Poiseuille flow, that is, $\tilde{\boldsymbol{u}} := \boldsymbol{u} - (1-s^2)\widehat{\boldsymbol{z}}$ which then satisfies homogeneous boundary conditions at the pipe wall and is presumed periodic along the pipe. The pressure p is already the 'perturbation' pressure and is strictly periodic to keep the applied pressure gradient fixed. The governing equations, (2.3) and (2.4), rewritten for these new variables and used henceforth are

$$\frac{\partial\tilde{\boldsymbol{u}}}{\partial t} + (1-s^2)\frac{\partial\tilde{\boldsymbol{u}}}{\partial z} - 2s\tilde{u}\widehat{\boldsymbol{z}} + \tilde{\boldsymbol{u}}\cdot\nabla\tilde{\boldsymbol{u}} + \nabla p - \frac{1}{Re}\nabla^2\tilde{\boldsymbol{u}} = \boldsymbol{0}, \tag{2.10}$$

$$\nabla\cdot\tilde{\boldsymbol{u}} = 0. \tag{2.11}$$

The nonlinear solutions found in this paper take the form of travelling waves which propagate at a constant speed and are therefore steady in an appropriate Galilean frame. This speed is expected to be non-zero due to the lack of fore–aft symmetry in pipe flow and represents an unknown emerging like an eigenvalue as part of the solution procedure. The travelling waves also possess a number of symmetries, the most important of which is a discrete m-fold rotational symmetry in the azimuthal direction ϕ so that the transformation

$$\mathscr{R}_m : (u, v, w, p)(s, \phi, z) \to (u, v, w, p)(s, \phi + 2\pi/m, z) \tag{2.12}$$

(in the usual cylindrical coordinates) leaves them unchanged for some integer m. This provides a natural partitioning and henceforth we shall refer to travelling waves with $\mathscr{R}_m$ symmetry as simply $\mathscr{R}_m$-waves. Properties of $\mathscr{R}_m$-waves with $m = 1, 2, 3, 4, 5$ and 6 will be described below but special attention will be devoted to illustrating how $\mathscr{R}_2$ and $\mathscr{R}_3$-waves were found since these appear first as Re increases.

3. The self-sustaining process (SSP)

There are three physical mechanisms and three distinct active velocity structures which come together to produce a self-sustained cycle. We look for a travelling wave solution or equivalently a steady solution in a frame moving at some constant speed

c in the streamwise z-direction. In this Galilean frame, a steady velocity field and pressure field can be decomposed without loss of generality into three parts

$$\begin{bmatrix}\tilde{\boldsymbol{u}}\\ p\end{bmatrix} = \begin{bmatrix}U(s,\phi)\\ V(s,\phi)\\ 0\\ P(s,\phi)\end{bmatrix}_{rolls} + \begin{bmatrix}0\\ 0\\ W(s,\phi)\\ 0\end{bmatrix}_{streaks} + \begin{bmatrix}\widehat{u}(s,\phi,z)\\ \widehat{v}(s,\phi,z)\\ \widehat{w}(s,\phi,z)\\ \widehat{p}(s,\phi,z)\end{bmatrix}_{waves} \tag{3.1}$$

where the various streamwise-independent and streamwise-dependent parts have been labelled 'rolls', 'streaks' and 'waves' respectively. For uniqueness, the waves have no mean under streamwise averaging, that is, $\overline{\tilde{\boldsymbol{u}}}^z = \boldsymbol{U}$ where

$$\overline{(\quad)}^z := \lim_{L\to\infty} \frac{1}{2L}\int_{-L}^{L} (\quad)\,\mathrm{d}z. \tag{3.2}$$

Also, formally, the term 'streak' usually refers to a fluctuation in the streamwise velocity away from a mean, $W(s,\phi) - \overline{W}(s)$ (where $\overline{W}(s)$ is the azimuthally averaged velocity). Here, as a convenient shorthand we refer to the whole spanwise-modulated shear flow $W(s,\phi)$ created by the rolls as the streak field.

In the absence of z-dependent waves, the streamwise rolls, $[U(s,\phi), V(s,\phi), 0]$, have no energy source and will secularly decay under viscosity. However before this can happen, they redistribute the mean shear to produce streaks, $W(s,\phi)$. This involves a considerable amplification in the overall disturbance to the flow, a general phenomenon in shear flows which has become known as 'transient growth' (Boberg & Brosa 1988; Bergström 1993; Schmid & Henningson 1994; O'Sullivan & Breuer 1994; Zikanov 1996). The process is simple to understand and linear in nature, depending only on the slow advection across a large mean shear sustained for a long time. In particular, if the streamwise rolls initially have amplitude $\epsilon \ll 1$, their viscous decay rate is $O(Re^{-1})$ and hence they survive over an $O(Re)$ timescale. During this period they can advect fluid across the $O(1)$ mean shear a distance $O(\epsilon Re)$ and thereby produce $O(\min(\epsilon Re, 1))$ streaks or azimuthal (spanwise) variations in the mean flow. In this way, an $O(\epsilon)$ disturbance can grow to an $O(\epsilon Re)$ level before ultimately decaying. This simple argument predicts $O(Re^2)$ growth in the disturbance energy at times of $O(Re)$ which is entirely consistent with detailed numerical computations of the transient growth linear problem (Schmid & Henningson 1994). The fact that the flow structure changes form – from rolls to streaks – during its evolution means that this effect cannot be captured using a traditional normal mode analysis but the flow still ultimately decays and does not contradict the fact that pipe flow is believed asymptotically (long-time) stable to all vanishingly small (linear) initial disturbances.

To close the cycle, there must be a three-dimensional wave field to feed energy back into the otherwise secularly decaying streamwise rolls. This can be produced naturally as a result of a linear instability of the streaks due to their spanwise inflectional structure. This phenomenon is now well known in plane channel flows (Hamilton *et al.* 1995; Waleffe 1995*a*, 1997; Reddy *et al.* 1998) and has been studied before in pipe flow (O'Sullivan & Breuer 1994; Zikanov 1996). Generically, one can imagine that the streaks need to be $O(1)$ before they become linearly unstable (or the most unstable streaks will be the strongest possible streaks which are $O(1)$) implying that the rolls are $O(Re^{-1})$. Then the nonlinear quadratic self-interaction of $O(Re^{-1})$ waves is sufficient to offset the viscous decay of these rolls. This simple picture suggests that the threshold amplitude for disturbances to trigger transition (i.e. the flow state moves permanently away from the laminar Hagen–Poiseuille solution) is bounded

m_0	$\lambda_{m_0 1}$	$\lambda_{m_0 2}$
1	5.1356223018	8.4172441404
2	6.3801618959	9.7610231300
3	7.5883424345	11.0647094885
4	8.7714838160	12.3386041975
5	9.9361095242	13.5892901705
6	11.0863200192	14.8212687270

TABLE 1. The decay rate eigenvalues, $J_{m_0+1}(\lambda_{m_0 n})=0$, for the streamwise roll structure in SSP.

above by $O(Re^{-1})$ (the correct scaling being given by the closest boundary of the basin of attraction of the Hagen–Poiseuille flow rather than the nearest alternative limit set). This precise scaling, however, seems confirmed by recent experimental work (Hof *et al.* 2003) and more careful asymptotic analysis (S. J. Chapman 2004, personal communication). The energetic feedback to the rolls is the essential nonlinear aspect of the cycle and since it is the most intricate and delicate to arrange must be considered the crucial link in the SSP advocated by Waleffe.

We now consider the SSP in detail to motivate the search for new solutions which follows in § 4.

3.1. *Choosing streamwise rolls*

The equations for the rolls are $\widehat{\boldsymbol{s}}\cdot\overline{(2.10)}^z$ and $\widehat{\boldsymbol{\phi}}\cdot\overline{(2.10)}^z$,

$$\partial_t U + P_s - \frac{1}{Re}\widehat{\boldsymbol{s}}\cdot\nabla^2\boldsymbol{U} = -\widehat{\boldsymbol{s}}\cdot(\boldsymbol{U}\cdot\nabla\boldsymbol{U} + \overline{\widehat{\boldsymbol{u}}\cdot\nabla\widehat{\boldsymbol{u}}}^z), \tag{3.3}$$

$$\partial_t V + \frac{1}{s}P_\phi - \frac{1}{Re}\widehat{\boldsymbol{\phi}}\cdot\nabla^2\boldsymbol{U} = -\widehat{\boldsymbol{\phi}}\cdot(\boldsymbol{U}\cdot\nabla\boldsymbol{U} + \overline{\widehat{\boldsymbol{u}}\cdot\nabla\widehat{\boldsymbol{u}}}^z), \tag{3.4}$$

together with the incompressibility condition $\partial_s(sU)+\partial V/\partial\phi=0$. These equations are independent of the streamwise velocity perturbation $W(s,\phi)\widehat{z}$. Linearizing completely (i.e. ignoring the right-hand sides of (3.3) and (3.4)), leads to the Stokesian problem for decaying streamwise structures. In the absence of a better alternative, the least decaying eigenfunction is a sensible choice as the initial streamwise structure. Hence setting λ^2/Re as the decay rate and without loss of generality choosing a single Fourier mode, $[U,V]=[U'(s)\cos m_0\phi, V'(s)\sin m_0\phi]$, the problem reduces to

$$\nabla^2(\nabla^2+\lambda^2)\left[(U'\pm \mathrm{i}V')\,\mathrm{e}^{\mathrm{i}(m_0\pm1)\phi}\right]=0. \tag{3.5}$$

At this point we are selecting a structure with $\mathscr{R}_{m_0}$ symmetry. This can always lead to travelling waves with the same symmetry (fundamental), a $\mathscr{R}_{m_0}$-wave, but other possibilities such as a (subharmonic) $\mathscr{R}_{m_0/2}$-wave if m_0 is even can occur too. The full solution is

$$U := \left[J_{m_0+1}(\lambda s)+J_{m_0-1}(\lambda s)-J_{m_0-1}(\lambda)s^{m_0-1}\right]\cos m_0\phi, \tag{3.6}$$

$$V := \left[J_{m_0+1}(\lambda s)-J_{m_0-1}(\lambda s)+J_{m_0-1}(\lambda)s^{m_0-1}\right]\sin m_0\phi, \tag{3.7}$$

with the eigenvalue condition that $J_{m_0+1}(\lambda)=0$ where J is the Bessel function of the first kind. Table 1 displays $\lambda_{m_0 n}$ for $m_0=1,\ldots,6$ and $n=1,2$ where $n-1$ is the number of zeros of the radial flow field $U'(s)$ in $0<s\leqslant 1$. In this paper $\lambda_{m_0 1}$ invariably proved successful to find fundamental modes whereas λ_{22} was used to find the $\mathscr{R}_1$ subharmonic wave. The rolls are presumed to have some amplitude ϵ defined as the maximum amplitude of the radial velocity U of the rolls.

3.2. *Formation of streaks*

The rolls advect the mean shear to produce high- and low-speed streaks $W(s,\phi)$ via the equation $\widehat{z}\cdot\overline{(2.10)}^{z}$

$$U\frac{\partial W}{\partial s}+\frac{V}{s}\frac{\partial W}{\partial \phi}-\frac{1}{Re}\nabla^2 W-2sU=-\overline{\widehat{\boldsymbol{u}}\cdot\nabla\widehat{w}}^{z}. \tag{3.8}$$

As the wave field $\widehat{\boldsymbol{u}}$ is currently unknown, the right-hand side of this equation is ignored before solving for W. The rolls as chosen enjoy two symmetries, one trivial and one non-trivial. Let $\mathscr{S}_1$ represent the rotate-and-reflect transformation

$$\mathscr{S}_1:(s,\phi,z)\to(-s,\phi+\pi,z),\qquad \mathscr{S}_1:(u,v,w,p)\to(-u,-v,w,p) \tag{3.9}$$

(since $\widehat{s}(-s,\phi+\pi)=-\widehat{s}(s,\phi)$ for example) and $\mathscr{Z}$ a reflection in the line $\phi=0$

$$\mathscr{Z}:(s,\phi,z)\to(s,-\phi,z),\qquad \mathscr{Z}:(u,v,w,p)\to(u,-v,w,p), \tag{3.10}$$

then

$$(U(\boldsymbol{x}),V(\boldsymbol{x}),0,P(\boldsymbol{x}))=\mathscr{S}_1\big(U\big(\mathscr{S}_1^{-1}\boldsymbol{x}\big),V\big(\mathscr{S}_1^{-1}\boldsymbol{x}\big),0,P\big(\mathscr{S}_1^{-1}\boldsymbol{x}\big)\big),$$
$$(U(\boldsymbol{x}),V(\boldsymbol{x}),0,P(\boldsymbol{x}))=\mathscr{Z}\big(U(\mathscr{Z}^{-1}\boldsymbol{x}),V(\mathscr{Z}^{-1}\boldsymbol{x}),0,P\big(\mathscr{S}_1^{-1}\boldsymbol{x}\big)\big).$$

From the streak equation (3.8), these roll symmetries carry over to the streaks. The former is a trivial symmetry of every flow field expressed in cylindrical polars because the coordinates (s,ϕ,z) and $(-s,\phi+\pi,z)$ represent the same point in physical space (e.g. see the Appendix of Kerswell & Davey 1996 for a discussion of this). This permits the streaks $W(s,\phi)$ to be represented efficiently as

$$W(s,\phi)=\sum_{m=0}^{M}W_m(s)\cos mm_0\phi \tag{3.11}$$

with the parity $W_m(-s)=(-1)^{mm_0}W_m(s)$. Figure 1 shows the streamwise rolls and associated streak structure at $(m_0=2, Re=1700, \alpha=1.55, \epsilon=7.1\times10^{-3})$ and $(m_0=3, Re=1800, \alpha=2.44, \epsilon=7.8\times10^{-3})$. Notice there are m_0 fast streaks near the pipe wall and m_0 slow streaks near the pipe centre. The cause of the streaks is clear: roll velocities towards (away from) the wall create fast (slow) streaks.

3.3. *Instability of streaks–waves*

At a certain amplitude ϵ of the rolls, the streaks become inflectionally unstable. Subtracting the parts of (2.10) which have been satisfied by defining the rolls and streaks leads to the wave equations

$$\frac{\partial\widehat{\boldsymbol{u}}}{\partial t}+(1-s^2)\frac{\partial\widehat{\boldsymbol{u}}}{\partial z}-2s\widehat{u}\,\widehat{\boldsymbol{z}}+\boldsymbol{U}\cdot\nabla\widehat{\boldsymbol{u}}+\widehat{\boldsymbol{u}}\cdot\nabla\boldsymbol{U}+\nabla\widehat{p}-\frac{1}{Re}\nabla^2\widehat{\boldsymbol{u}}$$
$$=-\widehat{\boldsymbol{u}}\cdot\nabla\widehat{\boldsymbol{u}}-\begin{bmatrix}\boldsymbol{U}\cdot\nabla U-V^2/s\\ \boldsymbol{U}\cdot\nabla V+UV/s\\ 0\end{bmatrix}, \tag{3.12}$$

$$\nabla\cdot\widehat{\boldsymbol{u}}=0 \tag{3.13}$$

(note this is not simply (2.10)–$\overline{(2.10)}^{z}$ since the roll equations solved are linearized). Dropping the right-hand side recovers the linear stability problem for a disturbance $\widehat{\boldsymbol{u}}$ superposed upon the rolls + streak flow $\boldsymbol{U}$. In contrast to Waleffe (1997), we include the rolls in the wave equations to keep as close as possible to the full Navier–Stokes

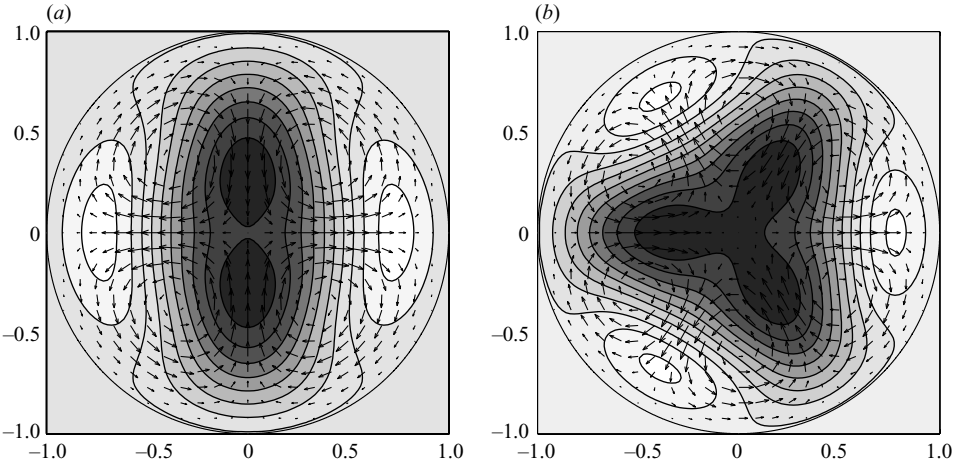

FIGURE 1. The two-dimensional streamwise rolls and streaks at $m_0 = 2$, $Re = 1700$, $\alpha = 1.55$, $\epsilon = 7.1 \times 10^{-3}$ (a) and at $m_0 = 3$, $Re = 1800$, $\alpha = 2.44$, $\epsilon = 7.8 \times 10^{-3}$ (b). The roll velocities are indicated by arrows and the shaded contours indicate the streak velocity W (the total axial speed with the laminar component subtracted). The shading scale is dark to light representing negative to positive velocities (the shade for zero is given by the pipe exterior). Notice that in the SSP solutions there are m_0 fast streaks near the wall and m_0 slow streaks near the pipe centre (obscured slightly by the choice of contour level for the $m_0 = 3$).

situation. However, this is not crucial since the mechanism for instability is the azimuthal (spanwise) inflections of the streak field and is only weakly modified by the presence of the rolls. To capture a steady solution in a travelling frame we are interested in finding waves which are marginally stable or neutral. Given the invariance of the wave equations to a translation in z, we can look for travelling Fourier modes in z, specifically $\widehat{\boldsymbol{u}}(\boldsymbol{x}, t) = \boldsymbol{u}(s, \phi)\, \mathrm{e}^{\mathrm{i}\alpha(z-ct)}$ where c is a complex eigenvalue (subsequently to be absorbed when purely real into a frame speed) and α is a real wavenumber. Since the rolls and streaks are invariant under the transformations $\mathscr{Z}$ and $\mathscr{S}_1$, as are the equations (3.12) and (3.13), the wave instability $\widehat{\boldsymbol{u}}$ can be partitioned into those which are either even or odd in the symmetry $\mathscr{Z}$, that is

$$(\widehat{u}(\boldsymbol{x}, t), \widehat{v}(\boldsymbol{x}, t), \widehat{w}(\boldsymbol{x}, t), \widehat{p}(\boldsymbol{x}, t)) = \pm\, \mathscr{Z}(\widehat{u}(\mathscr{Z}^{-1}\boldsymbol{x}, t), \widehat{v}(\mathscr{Z}^{-1}\boldsymbol{x}, t), \widehat{w}(\mathscr{Z}^{-1}\boldsymbol{x}, t), \widehat{p}(\mathscr{Z}^{-1}\boldsymbol{x}, t)) \tag{3.14}$$

(the disturbances must be symmetric or invariant under $\mathscr{S}_1$). We shall refer to these as $\mathscr{Z}$-even or $\mathscr{Z}$-odd modes. Given the z-periodic ansatz for $\widehat{\boldsymbol{u}}$, an alternative symmetry called a 'shift-and-reflect' symmetry $\mathscr{S}_2$ defined as

$$\mathscr{S}_2 : (s, \phi, z) \to (s, -\phi, z + \pi/\alpha), \qquad \mathscr{S}_2 : (u, v, w, p) \to (u, -v, w, p) \tag{3.15}$$

leads to an identical partitioning. This symmetry is trivially satisfied by the underlying flow $\boldsymbol{U}$ since $\mathscr{S}_2$ acts like $\mathscr{Z}$ on z-independent velocity fields and is admitted by (3.12) and (3.13). The disturbance $\widehat{\boldsymbol{u}}(\boldsymbol{x}, t)$ can either be invariant or symmetric ($\mathscr{S}_2$-even) under the transformation $\mathscr{S}_2$ or flipped in sign and antisymmetric ($\mathscr{S}_2$-odd). At this stage when we are considering just the initial instability (i.e. just one mode in z), introducing the transformation $\mathscr{S}_2$ seems redundant since an $\mathscr{R}$-even mode is an $\mathscr{S}_2$-odd mode and an $\mathscr{R}$-odd mode is an $\mathscr{S}_2$-even mode. However when we need to consider all the higher harmonics generated by the initial instability then possessing both symmetries is crucial for efficient representation of the solution. This is because

the base state (rolls+streaks) is both $\mathscr{R}$-even and $\mathscr{S}_2$-even. Consequently, an $\mathscr{R}$-even instability will generate $\mathscr{R}$-even higher harmonics only and an $\mathscr{S}_2$-even instability will generate $\mathscr{S}_2$-even higher harmonics only. This means that we can capture the full nonlinear solution emerging from an $\mathscr{R}$-even bifurcation within the space of $\mathscr{R}$-even flows and the full nonlinear solution emerging from an $\mathscr{R}$-odd bifurcation (i.e. an $\mathscr{S}_2$-even bifurcation) within the space of $\mathscr{S}_2$-even flows. This realization is crucial for achieving the required levels of truncation within given computational constraints.

One final remark is due regarding the m_0-fold periodicity in ϕ of the rolls+streaks. There will be *fundamental* disturbances possessing the same periodicity and *non-fundamental* disturbances which take the form $\hat{\boldsymbol{u}}(s,\phi,z)=\boldsymbol{v}(s,\phi,z)\,\mathrm{e}^{\mathrm{i}m\phi}$ where $0<m<m_0$ is an integer and $\boldsymbol{v}$ is m_0-fold periodic. In this work, the only non-fundamental disturbances considered will be the simplest subharmonic disturbances where $m=m_0/2$ which only exist if m_0 is even. These will be $\mathscr{R}_{m_0/2}$-waves. In summary, we can use the following representations of $\hat{\boldsymbol{u}}$ to capture the main forms of instability. Fundamental modes are

$$\begin{bmatrix}\hat{u}\\ \hat{v}\\ \hat{w}\\ \hat{p}\end{bmatrix}=\sum_{n=0}^{N-1}\sum_{m=0}^{M}\begin{bmatrix}u_{nm}\Theta_n(s;mm_0)\cos mm_0\phi\\ v_{nm}\Theta_n(s;mm_0)\sin mm_0\phi\\ w_{nm}\Phi_n(s;mm_0)\cos mm_0\phi\\ p_{nm}\Psi_n(s;mm_0)\cos mm_0\phi\end{bmatrix}\mathrm{e}^{\mathrm{i}\alpha(z-ct)},\qquad \mathscr{Z}\text{-even},\tag{3.16}$$

$$\begin{bmatrix}\hat{u}\\ \hat{v}\\ \hat{w}\\ \hat{p}\end{bmatrix}=\sum_{n=0}^{N-1}\sum_{m=0}^{M}\begin{bmatrix}u_{nm}\Theta_n(s;mm_0)\sin mm_0\phi\\ v_{nm}\Theta_n(s;mm_0)\cos mm_0\phi\\ w_{nm}\Phi_n(s;mm_0)\sin mm_0\phi\\ p_{nm}\Psi_n(s;mm_0)\sin mm_0\phi\end{bmatrix}\mathrm{e}^{\mathrm{i}\alpha(z-ct)},\qquad \mathscr{S}_2\text{-even},\tag{3.17}$$

and, if m_0 is even, the subharmonic modes are

$$\begin{bmatrix}\hat{u}\\ \hat{v}\\ \hat{w}\\ \hat{p}\end{bmatrix}=\sum_{n=0}^{N-1}\sum_{m=0}^{M-1}\begin{bmatrix}u_{nm}\Theta_n\big(s;(m+\frac12)m_0\big)\cos\big[(m+\frac12)m_0\phi\big]\\ v_{nm}\Theta_n\big(s;(m+\frac12)m_0\big)\sin\big[(m+\frac12)m_0\phi\big]\\ w_{nm}\Phi_n\big(s;(m+\frac12)m_0\big)\cos\big[(m+\frac12)m_0\phi\big]\\ p_{nm}\Psi_n\big(s;(m+\frac12)m_0\big)\cos\big[(m+\frac12)m_0\phi\big]\end{bmatrix}\mathrm{e}^{\mathrm{i}\alpha(z-ct)},\quad \mathscr{Z}\text{-even},\tag{3.18}$$

$$\begin{bmatrix}\hat{u}\\ \hat{v}\\ \hat{w}\\ \hat{p}\end{bmatrix}=\sum_{n=0}^{N-1}\sum_{m=0}^{M-1}\begin{bmatrix}u_{nm}\Theta_n\big(s;(m+\frac12)m_0\big)\sin\big[(m+\frac12)m_0\phi\big]\\ v_{nm}\Theta_n\big(s;(m+\frac12)m_0\big)\cos\big[(m+\frac12)m_0\phi\big]\\ w_{nm}\Phi_n\big(s;(m+\frac12)m_0\big)\sin\big[(m+\frac12)m_0\phi\big]\\ p_{nm}\Psi_n\big(s;(m+\frac12)m_0\big)\sin\big[(m+\frac12)m_0\phi\big]\end{bmatrix}\mathrm{e}^{\mathrm{i}\alpha(z-ct)},\quad \mathscr{S}_2\text{-even}.\tag{3.19}$$

Here

$$\Psi_n(s;i):=\begin{cases}T_{2n+1}(s), & i\ \text{odd},\\ T_{2n}(s), & i\ \text{even},\end{cases}\qquad \Theta_n(s;i):=\begin{cases}T_{2n+2}(s)-T_{2n}(s), & i\ \text{odd},\\ T_{2n+3}(s)-T_{2n+1}(s), & i\ \text{even},\end{cases}\tag{3.20}$$

$$\Phi_n(s;i):=\begin{cases}T_{2n+3}(s)-T_{2n+1}(s), & i\ \text{odd},\\ T_{2n+2}(s)-T_{2n}(s), & i\ \text{even},\end{cases}\tag{3.21}$$

where $T_n(s):=\cos(n\cos^{-1}s)$ is the nth Chebyshev polynomial so that the boundary conditions are built into the spectral functions. In this paper, we confine our attention solely to fundamental and subharmonic $\mathscr{S}_2$-even solutions (waves derived from wave instabilities of form (3.17) and (3.19)). Preliminary calculations indicated that these were the first to appear for the chosen rolls. Future work will explore the $\mathscr{Z}$-even solutions.

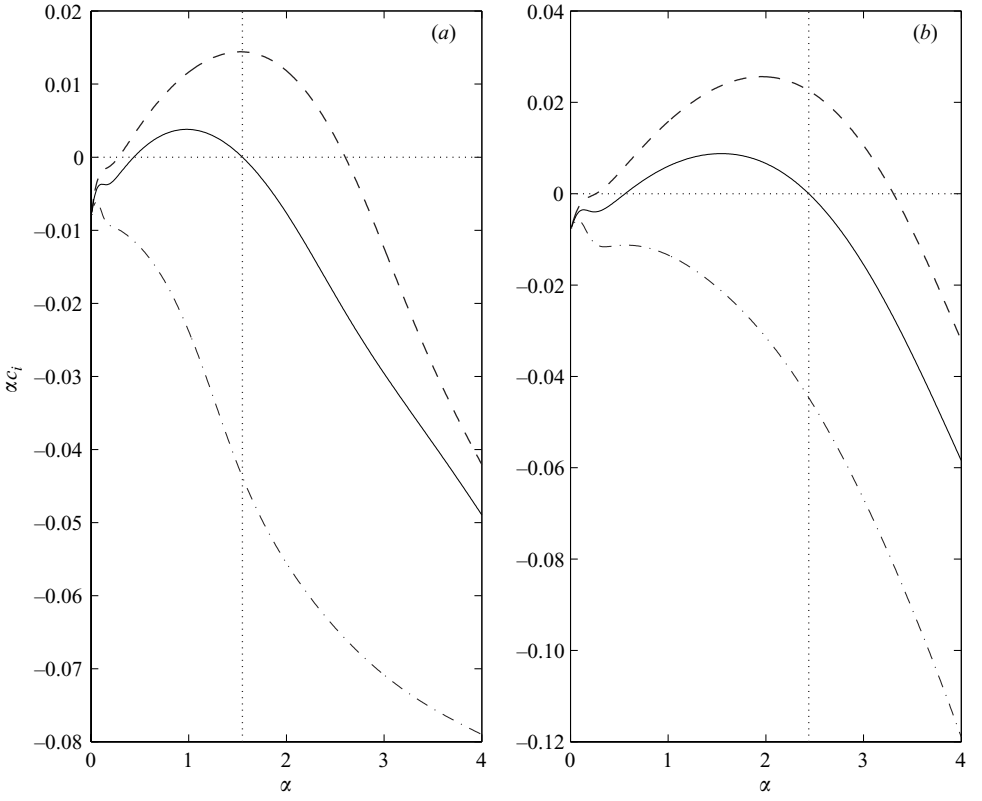

FIGURE 2. Streak instability growth rates αc_i (where c_i is the imaginary part of c) as a function of α and the roll amplitude ϵ. (*a*) $m_0 = 2$, $Re = 1700$ and roll amplitude $\epsilon = 0.009188$ (dashed), $\epsilon = 0.00711$ (solid) and $\epsilon = 0.005011$ (dash-dot). The vertical dotted line indicates the neutral wave mode at $\alpha = 1.55$. (*b*) $m_0 = 3$, $Re = 1800$ and roll amplitude $\epsilon = 0.00938$ (dashed), $\epsilon = 0.0078$ (solid) and $\epsilon = 0.00625$ (dash-dot). The vertical dotted line indicates the neutral wave mode at $\alpha = 2.44$.

Figure 2 shows typical streak instability profiles over wavenumber α for $m_0 = 2$ and 3. If the rolls are weaker than a threshold there is no streak instability. Beyond this, there are two neutral waves with the one at higher wavenumber giving by far the better feedback.

3.4. *Nonlinear feedback to the rolls*

As already mentioned, the crucial link in the SSP cycle is the nonlinear feedback of the waves to the rolls. To assess this, the roll component of the form $(U'(s)\cos m_0\phi, V'(s)\sin m_0\phi, 0)$ which would be induced by the waves $\widehat{\boldsymbol{u}}$ (through the right-hand sides of (3.3) and (3.4)) is calculated. The key issue is to establish whether the shape of these induced rolls matches that of the imposed rolls already in place (as given by (3.6)). If there is significant overlap of structure then finite-amplitude versions of these waves can be expected to sustain the rolls against secular viscous decay. The amplitude of the waves, which formally completes the 'SSP' approximate solution, is presumed set by this precise balancing and as a result is typically $O(\sqrt{\epsilon/Re})$.

To examine the feedback of a wave instability, we compare the radial velocity $U'(s)$ of the induced rolls with that of the imposed rolls. Applying $\widehat{\boldsymbol{s}}\cdot\nabla\times\nabla\times$ to the equation

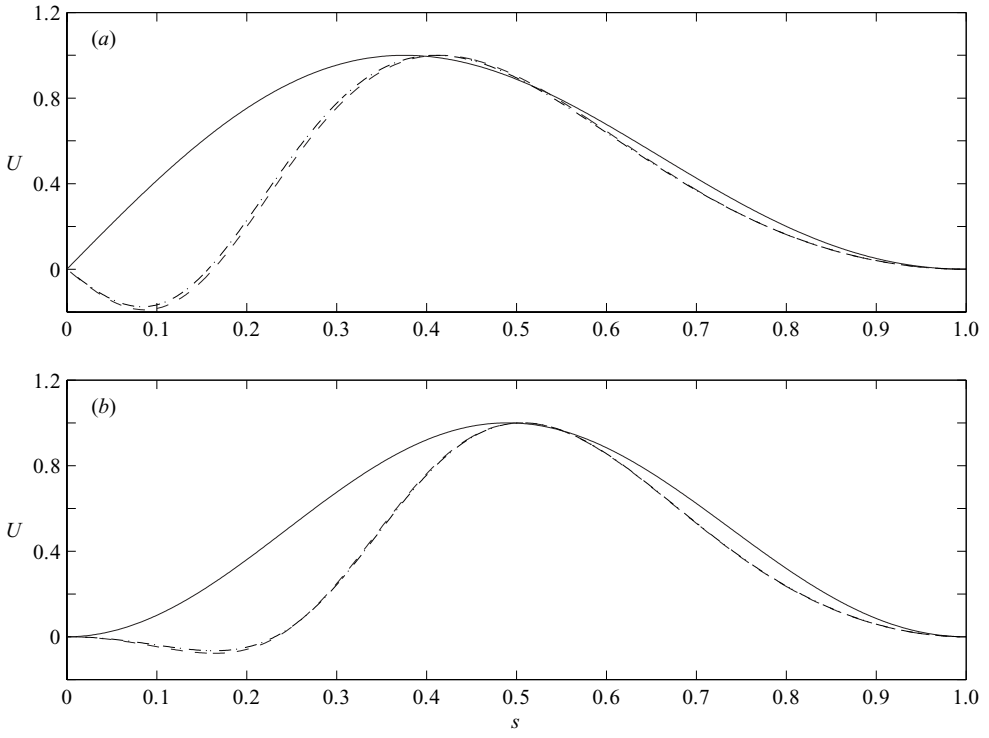

FIGURE 3. Plots showing good feedback. The radial velocity component of the imposed rolls is plotted with the induced radial velocity component $U'(s)$ as calculated from (3.22) and normalized appropriately. (*a*) $U'(s)$ at $Re = 1700$ (dashed) and $Re = 2100$ (dot-dash) corresponding to the first $\mathscr{S}_2$-symmetric wave instability compared with the radial component of the original rolls (solid) for $m_0 = 2$ ($\alpha = 1.55$). (*b*) $U'(s)$ at $Re = 1800$ (dashed) and $Re = 2200$ (dot-dash) corresponding to the first $\mathscr{S}_2$-symmetric wave instability compared with the radial component of the original rolls (solid) for $m_0 = 3$ ($\alpha = 2.44$).

pair (3.3)–(3.4) leads to a single equation for the radial roll velocity

$$\frac{1}{Re}\left(\nabla^2 + \frac{2}{s}\frac{\partial}{\partial s} + \frac{1}{s^2}\right)^2 U = \hat{\boldsymbol{s}}\cdot\nabla\times\nabla\times(\overline{\hat{\boldsymbol{u}}\cdot\nabla\hat{\boldsymbol{u}}}^z) \tag{3.22}$$

where the nonlinear roll terms are ignored due to their small amplitude. Only the projection of the right-hand side onto $\cos m_0\phi$ is used when inverting the linear operator to calculate $U'(s)$. A successful match (to be interpreted as significant overlap of profiles as for example displayed in figure 3) indicates that the imposed streamwise rolls of amplitude ϵ, the associated streaks and the wave disturbance of some small amplitude set by roll energetic considerations constitutes a 'SSP' solution. The importance of such a 'solution' is that it gives an approximate location in parameter space in which to search for an exact travelling wave solution using the smooth continuation approach described in the following section. In particular, information carried over to that analysis is the form of the initial rolls, their amplitude ϵ, the Reynolds number and the axial wavenumber α for the wave instability. In practice, a subcritical bifurcation is always found close to that predicted by the SSP analysis. However, there is no guarantee that this new solution branch can be continued back to the zero-forcing situation. Typically, this can be engineered by increasing Re as will

be discussed below. Figure 3 shows typical feedbacks which were considered good enough to launch a more in-depth search for a travelling wave solution via techniques described below.

4. Exact solutions via smooth continuation

The key idea to convert the approximate analysis of the SSP to a more formal continuation setting is to add a body forcing to the Navier–Stokes equations (Waleffe 1998). This body force is designed to initially maintain the streamwise rolls considered in the SSP analysis against viscous decay in the absence of any other flow structures. Since these rolls were simply the least decaying eigenmodes of the linearized Stokesian operator (as given in (3.3) and (3.4)), the forcing function mirrors their structure. Specifically, the new roll equations are

$$\partial_t U + P_s - \frac{1}{Re}\widehat{\boldsymbol{s}}\cdot\nabla^2\boldsymbol{U} + \widehat{\boldsymbol{s}}\cdot(\boldsymbol{U}\cdot\nabla\boldsymbol{U}) = f_s(s,\phi) - \widehat{\boldsymbol{s}}\cdot(\overline{\widehat{\boldsymbol{u}}\cdot\nabla\widehat{\boldsymbol{u}}}^z), \tag{4.1}$$

$$\partial_t V + \frac{1}{s}P_\phi - \frac{1}{Re}\widehat{\boldsymbol{\phi}}\cdot\nabla^2\boldsymbol{U} + \widehat{\boldsymbol{\phi}}\cdot(\boldsymbol{U}\cdot\nabla\boldsymbol{U}) = f_\phi(s,\phi) - \widehat{\boldsymbol{\phi}}\cdot(\overline{\widehat{\boldsymbol{u}}\cdot\nabla\widehat{\boldsymbol{u}}}^z), \tag{4.2}$$

where

$$\left.\begin{aligned} f_s(s,\phi) &:= 2A\left[J_{m_0+1}(\lambda s) + J_{m_0-1}(\lambda s) - J_{m_0-1}(\lambda)s^{m_0-1}\right]\cos m_0\phi,\\ f_\phi(s,\phi) &:= 2A\left[J_{m_0+1}(\lambda s) - J_{m_0-1}(\lambda s) + J_{m_0-1}(\lambda)s^{m_0-1}\right]\sin m_0\phi,\end{aligned}\right\} \tag{4.3}$$

and A measures the forcing amplitude. Since the streamwise roll amplitude ϵ has been defined as the maximum value of the radial velocity component, then ignoring the nonlinear roll term (that is assuming $\epsilon \ll 1$), the forced rolls have amplitude

$$\epsilon = \frac{2ARe}{\lambda^2} \times \max_{s\in[0,1]}\left[J_{m_0+1}(\lambda s) + J_{m_0-1}(\lambda s) - J_{m_0-1}(\lambda)s^{m_0-1}\right]. \tag{4.4}$$

If the forcing A goes beyond a threshold amplitude, a symmetry-breaking, three-dimensional streak instability will occur as predicted by the SSP analysis near the appropriate streamwise wavenumber α. The fact that this instability is known to have positive feedback to the rolls makes it very likely (but not certain) that this bifurcation will be subcritical. (Considering the feedback to the rolls only captures one half of the weakly nonlinear processes near the bifurcation since the excitation of the second harmonic is ignored. However, in our experience in this problem the former physics always dominates the latter and so finding positive feedback invariably implies subcriticality of the wave bifurcation.) Given this subcriticality, following the new solution branch corresponds to decreasing the forcing amplitude as the wave increasingly takes over the role of maintaining the rolls. In other words, as the wave amplitude grows along the solution branch, the two components of $\overline{\widehat{\boldsymbol{u}}\cdot\nabla\widehat{\boldsymbol{u}}}^z$ take over the role of (f_s, f_ϕ) in (4.1) and (4.2) of sustaining the rolls. Ideally, the forcing amplitude can be reduced to zero at which point a fully nonlinear travelling solution to the physical pipe flow problem has been achieved. The SSP analysis merely isolates excellent candidates for continuation: it can say nothing about whether the continuation will ultimately cross the $A=0$ axis. By way of illustration, it is possible to construct SSP solutions down to $Re \approx 500$ whereas the travelling waves are only found to exist for $Re \geqslant 1600$. If the Re is too low the solution branch reaches a minimum positive A before bending back to move towards increasing values of A. However, continuing the branch to higher Re invariably moves this minimum through the $A=0$ axis with the one notable exception of the fundamental $\mathscr{S}_2$-even $m_0=1$

case. No travelling solution of this type was found to cross the $A=0$ axis below $Re=6000$ despite starting with an SSP solution exhibiting excellent feedback (Faisst & Eckhardt (2003) also report a similar failure to find this mode).

4.1. *Numerical formulation*

The problem (2.10) (with body force $\boldsymbol{f}=f_s(s,\phi)\widehat{\boldsymbol{s}}+f_\phi(s,\phi)\widehat{\boldsymbol{\phi}}$ added) and (2.11) was solved as stated – three momentum + one continuity equations – in terms of the primitive variables $(\tilde{u},\tilde{v},\tilde{w},\tilde{p})$ rather than any reduced representation of the velocity field such as a poloidal–toroidal decomposition. Experience indicates that this provides the best numerically conditioned formulation since spatial derivatives are kept at their lowest order. The governing equations were imposed by collocation over s and Galerkin projection over ϕ and z. The axis of the pipe can cause numerical problems unless specific efforts are made to desensitize the code to this artificial singularity. This was achieved here by exploiting the representation degeneracy of cylindrical polar coordinates in which the points $(-s,\phi\pm\pi,z)$ and (s,ϕ,z) are exactly equivalent. This means that each velocity component and scalar pressure function has a definite parity in s determined by whether its corresponding azimuthal wavenumber m is even or odd (see the Appendix of Kerswell & Davey 1996). Building the appropriate radial parity into the spectral representation of each field variable not only saves on storage but automatically instils the correct limiting behaviour near the axis. Computationally, we consider the domain $\{-1\leqslant s\leqslant 1, 0\leqslant\phi<\pi\}$ rather than viewing the interior of the pipe as the region $\{0\leqslant s\leqslant 1,-\pi\leqslant\phi<\pi\}$. The solution in $-1\leqslant s<0$ can be constructed from that in $0<s\leqslant 1$ through the known symmetries and so we need only collocate the equations over the positive zeros of $T_{2N}(s)$ and impose boundary conditions at $s=1$. Most importantly, this means that the collocation points are at their sparsest near the axis – $O(1/2N)$ spacing – and at their densest – $O(1/4N^2)$ spacing – near the sidewall where boundary layers typically need to be resolved.

Two types of travelling wave solutions were sought: fundamental $\mathscr{S}_2$-even solutions of the form

$$\begin{bmatrix}\tilde{u}\\ \tilde{v}\\ \tilde{w}\\ \tilde{p}\end{bmatrix}=\sum_{n=0}^{N-1}\sum_{m=0}^{M}\left\{\sum_{l=1,l\,odd}^{L}\begin{bmatrix}u_{nml}\Theta_n(s;mm_0)\sin mm_0\phi\\ v_{nml}\Theta_n(s;mm_0)\cos mm_0\phi\\ w_{nml}\Phi_n(s;mm_0)\sin mm_0\phi\\ p_{nml}\Psi_n(s;mm_0)\sin mm_0\phi\end{bmatrix}\mathrm{e}^{\mathrm{i}\alpha l(z-ct)}\right.$$
$$\left.+\sum_{l=0,l\,even}^{L}\begin{bmatrix}u_{nml}\Theta_n(s;mm_0)\cos mm_0\phi\\ v_{nml}\Theta_n(s;mm_0)\sin mm_0\phi\\ w_{nml}\Phi_n(s;mm_0)\cos mm_0\phi\\ p_{nml}\Psi_n(s;mm_0)\cos mm_0\phi\end{bmatrix}\mathrm{e}^{\mathrm{i}\alpha l(z-ct)}\right\}+\text{c.c.}$$

and, if m_0 is even, subharmonic $\mathscr{S}_2$-even solutions of the form

$$\begin{bmatrix}\tilde{u}\\ \tilde{v}\\ \tilde{w}\\ \tilde{p}\end{bmatrix}=\sum_{n=0}^{N-1}\left\{\sum_{m=0,m\,even}^{2M}\sum_{l=0,l\,even}^{L}\begin{bmatrix}u_{nml}\Theta_n\left(s;\tfrac{1}{2}mm_0\right)\cos\tfrac{1}{2}mm_0\phi\\ v_{nml}\Theta_n\left(s;\tfrac{1}{2}mm_0\right)\sin\tfrac{1}{2}mm_0\phi\\ w_{nml}\Phi_n\left(s;\tfrac{1}{2}mm_0\right)\cos\tfrac{1}{2}mm_0\phi\\ p_{nml}\Psi_n\left(s;\tfrac{1}{2}mm_0\right)\cos\tfrac{1}{2}mm_0\phi\end{bmatrix}\mathrm{e}^{\mathrm{i}\alpha l(z-ct)}\right.$$
$$\left.+\sum_{m=1,m\,odd}^{2M-1}\sum_{l=1,l\,odd}^{L}\begin{bmatrix}u_{nml}\Theta_n\left(s;\tfrac{1}{2}mm_0\right)\sin\tfrac{1}{2}mm_0\phi\\ v_{nml}\Theta_n\left(s;\tfrac{1}{2}mm_0\right)\cos\tfrac{1}{2}mm_0\phi\\ w_{nml}\Phi_n\left(s;\tfrac{1}{2}mm_0\right)\sin\tfrac{1}{2}mm_0\phi\\ p_{nml}\Psi_n\left(s;\tfrac{1}{2}mm_0\right)\sin\tfrac{1}{2}mm_0\phi\end{bmatrix}\mathrm{e}^{\mathrm{i}\alpha l(z-ct)}\right\}+\text{c.c.}$$

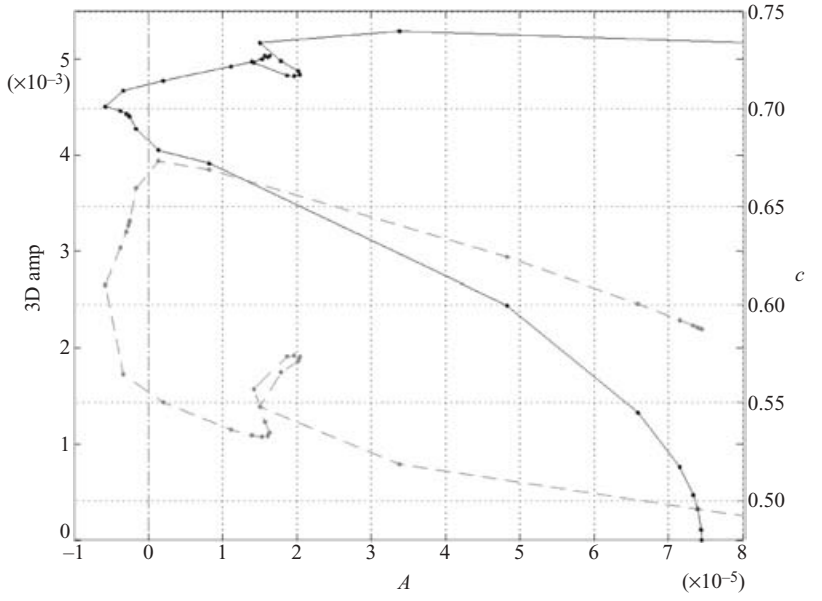

FIGURE 4. The continuation curve for $m_0 = 2, \alpha = 1.55$ at $Re = 2100$ (truncation (8, 25, 5)). The solid line shows how the forcing amplitude A can be decreased from $A_{crit} = 7.44 \times 10^{-5}$ as a three-dimensional (3D) amplitude measure increases (note the parabolic head indicative of a subcritical bifurcation). There are two crossings of the pipe flow limit ($A = 0$) representing an upper and lower branch of travelling wave solutions. The dashed line shows that the lower branch has faster travelling waves than the upper branch. The dots show specific convergences of the path-finding procedure indicating how easy or difficult the solution is to follow.

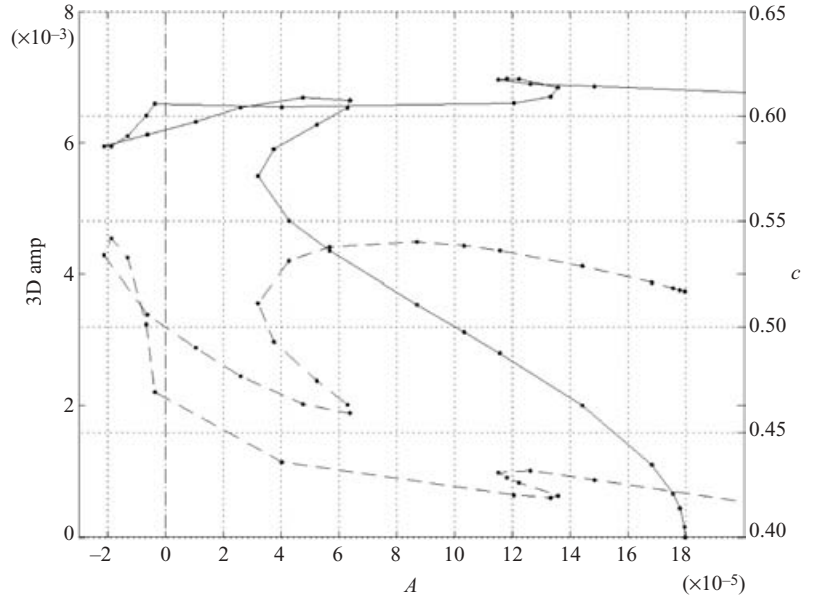

FIGURE 5. The continuation curve for $m_0 = 3, \alpha = 2.44$ at $Re = 1800$ ($A_{crit} = 1.7962 \times 10^{-4}$ as opposed to $A_{crit} = 1.75 \times 10^{-4}$ predicted from the SSP analysis: truncation (8, 24, 5)). Again there are two crossings of the pipe flow limit ($A = 0$) representing an upper and lower branch of travelling wave solutions.

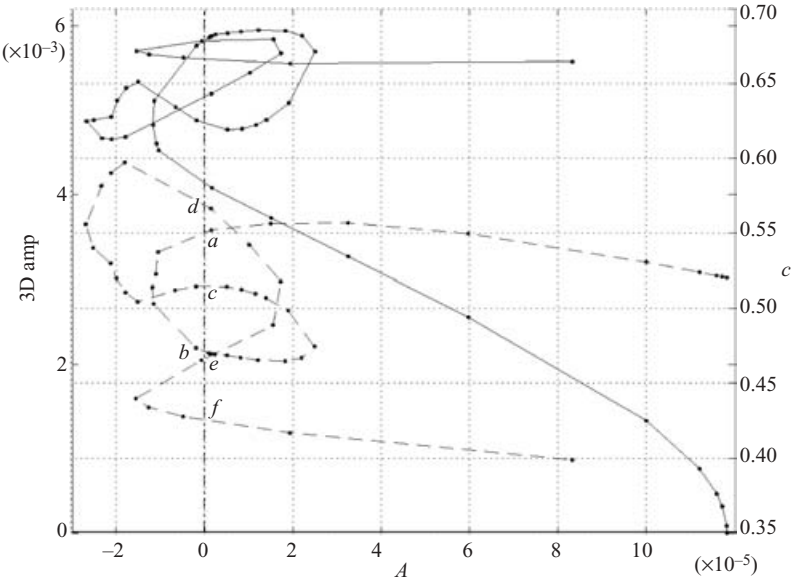

FIGURE 6. The continuation curve for $m_0 = 3, \alpha = 2.44$ at $Re = 2200$ ($A_{crit} = 1.182 \times 10^{-4}$, truncation (8, 24, 5)). Now we are sufficiently away from the saddle-node bifurcation point to find more complicated behaviour. There are six crossings of $A = 0$ indicating six travelling wave solutions at this α and Re value! The various crossings have been labelled a to f for referencing in figures 7 and 8.

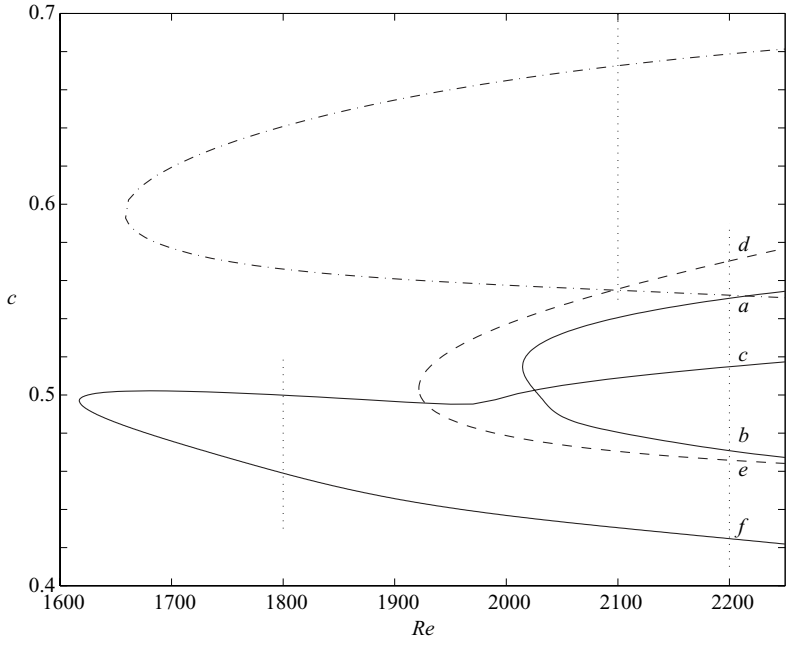

FIGURE 7. The travelling wave solution curves traced out by taking the solutions found from the continuations reported in figures 4 (truncation (8, 25, 5)), 5 and 6 (both at truncation (8, 24, 5)). The $m_0 = 2$ dash-dot curve ($\alpha = 1.55$) is one pair of upper and lower branches corresponding to a saddle-node bifurcation at lower Re. In contrast there are multiple $m_0 = 3$ curves (solid and dashed) at $\alpha = 2.44$. The labelling (a to f) used in figure 6 is reproduced here to indicate the correspondence between the crossings and the various branches. Note that the apparent crossings of the $m_0 = 3$ curves are due to projection onto a plane and not bifurcations.

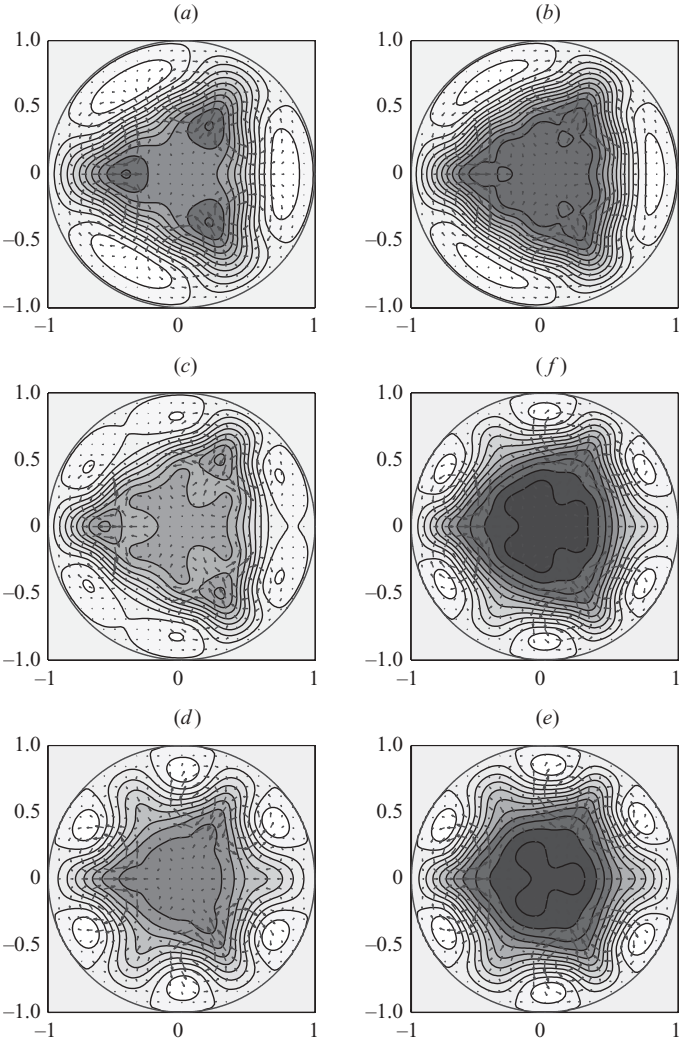

FIGURE 8. Streamwise-averaged plots of the various solutions labelled in figure 6 to show their different streak structure. The arrows indicate the streamwise-averaged cross-stream velocities $\overline{\boldsymbol{v}_\perp}^z$ (larger arrows corresponding to larger speeds) and the shading represents the streamwise-averaged axial velocity differential, $\overline{\tilde{w}}^z$ (dark most negative and light most positive; the shading of the area exterior to the pipe represents zero). Solutions are arranged in branch pairings – *a* and *b*, *c* and *f*, and *d* and *e* – and so that the respective upper (lower) branch solution (referring to figure 7) is on the left (right). Since all solutions correspond to $Re = 2200$ the contour levels are kept constant across the figures (from -0.5 to 0.5 in steps of 0.031) to highlight their relative magnitude of $\overline{\tilde{w}}^z$. Quantitatively, $(\min(\overline{\tilde{w}}^z), \max(\overline{\tilde{w}}^z), \max(|\overline{\boldsymbol{v}_\perp}^z|)) = (-0.31, 0.057, 0.011)$ for *a*, $(-0.33, 0.047, 0.018)$ for *b*, $(-0.25, 0.037, 0.015)$ for *c*, $(-0.28, 0.065, 0.013)$ for *d*, $(-0.39, 0.068, 0.017)$ for *e* and $(-0.40, 0.059, 0.020)$ for *f* (a speed of 1 corresponds to the centreline speed of the laminar solution at a Reynolds number of *Re*).

where α is the primary axial wavenumber. As before, the appropriate boundary conditions are built directly into the spectral expansion functions (see (3.20) and (3.21)). For a given truncation (M, N, L), there were $2N(4ML + 4M + 4L + 1)$ real coefficients to be determined for the fundamental solution and $2N(4ML + 4M + 2L \pm 1)$ in the

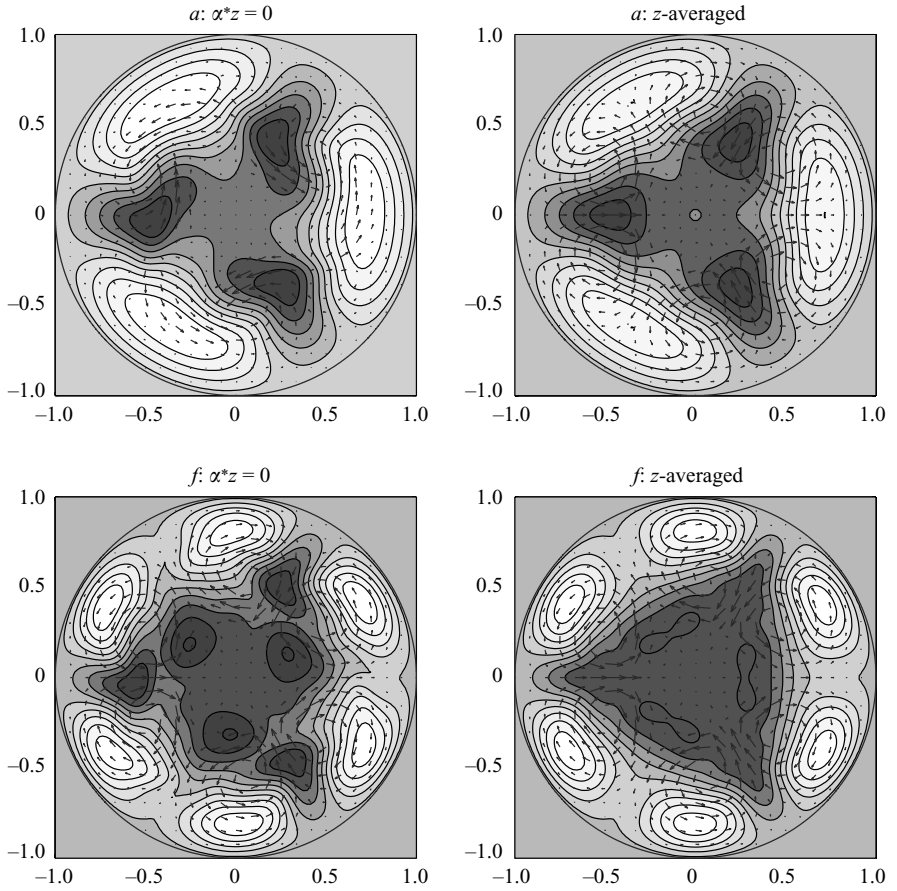

FIGURE 9. Velocity fields for the $\mathscr{R}_3$ solutions a (upper) and f (lower) of figure 7. The left plots are contour plots of $w_m = \tilde{w} + (1 - Re_m/Re)(1 - s^2)$ and arrow plots of the cross-stream velocity at a given z-station along the pipe (arbitrarily chosen as $z = 0$). The right plots are the z-average of w_m and the cross-stream velocity along the pipe. There are 10 contour levels in the upper plots ranging from -0.18 to 0.14 and 10 contour levels in the lower plots ranging from -0.14 to 0.16. These plots illustrate how the fast streaks near the wall are effectively two-dimensional whereas the slow interior streaks can have an appreciable three-dimensional element. The slow streaks only oscillate slightly in space in the upper solution a as evidenced in the fairly close match with the streamwise-averaged field. In contrast, there is much more variation in the interior of solution f where the streamwise-average looks featureless but a typical slice has six well-defined slow streaks. Subtracting the equivalent laminar flow of the same mass flux leads to clearer visualization of the slower fluid velocities near the centre of the pipe: compare these averaged plots with those of figure 8.

subharmonic case ($+/-$ corresponding to L even/odd). One further equation,

$$\mathrm{Im}\left\{\sum_{n=0}^{N-1} u_{n-11}\Theta_n(0.1; -m_0)\right\} = 0, \tag{4.5}$$

was imposed to eliminate the phase degeneracy of the travelling wave and served to determine the wave speed c. The resultant nonlinear algebraic system,

$$\mathscr{F}(u_{lmn}, v_{lmn}, w_{lmn}, p_{lmn}, c; Re, A, \alpha) = \mathbf{0}, \tag{4.6}$$

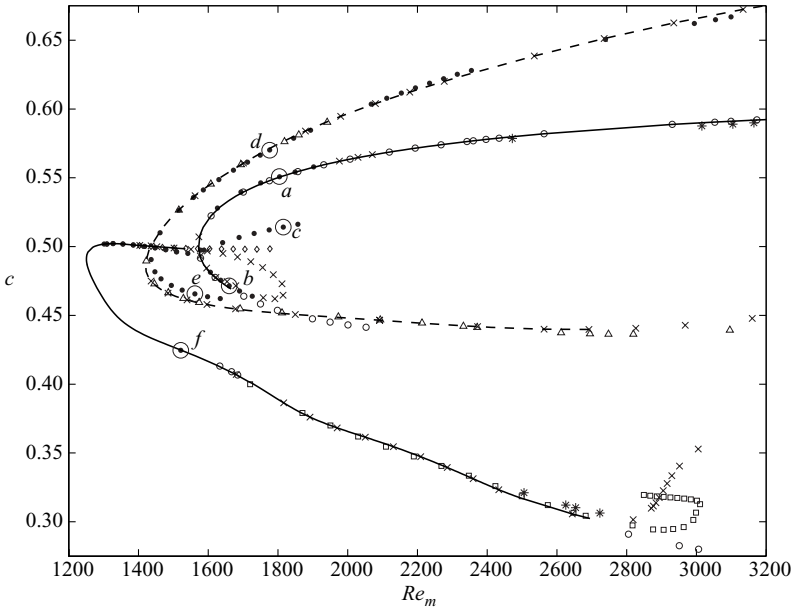

FIGURE 10. An exploration of numerical convergence for the multiple solution branches for $\mathscr{R}_3$ revealed in figure 7. The solutions a–f at $Re = 2200$ are marked as in figure 7 but now over Re_m. A solid or dashed line indicates where a solution branch has been confirmed by different truncation levels (the dashed line corresponds to the dashed line in figure 7). This shows that the $(8, 24, 5)$ solutions a, b, d, e and f are real (although e is poorly resolved) and that c is a numerical artefact. Notice that $(9, 26, 6)$ indicates that there are two separate branches. The truncation levels (M, N, L) used are ● $(8, 24, 5)$, ∗ $(8, 24, 6)$, □ $(8, 24, 7)$, ◇ $(8, 26, 5)$, × $(9, 26, 6)$, △ $(8, 28, 6)$, ○ $(9, 28, 5)$.

was solved given a nearby starting solution using the *PITCON* package developed by Rheinboldt & Burkardt (1983*a*, *b*) which is a robust branch-following program based upon Newton–Raphson iteration. Typically up to 16 000 degrees of freedom were used (requiring sub-2GB storage) but occasionally up to 20 000 degrees of freedom (3GB storage) were used to confirm convergence.

5. Results

5.1. *Searching for travelling waves*

The search for SSP solutions proceeded by first choosing m_0, selecting the least decaying streamwise rolls and then adjusting their amplitude ϵ until the streak field became unstable at a given Reynolds number Re and axial wavelength α. The feedback associated with this wave instability was then checked for compatibility with the initial rolls. If the match was very good (i.e. there was a strong positive correlation between the structure of the induced and imposed rolls), this set of parameters $(m_0, \lambda_{m_0 1}, \epsilon, Re, \alpha)$ was used as a starting point in parameter space to initiate the smooth continuation procedure of § 4. If instead the match was poor, indicated by a negative correlation between the radial velocity components of induced and imposed rolls, a number of corrective strategies could be employed: vary Re, increase ϵ further

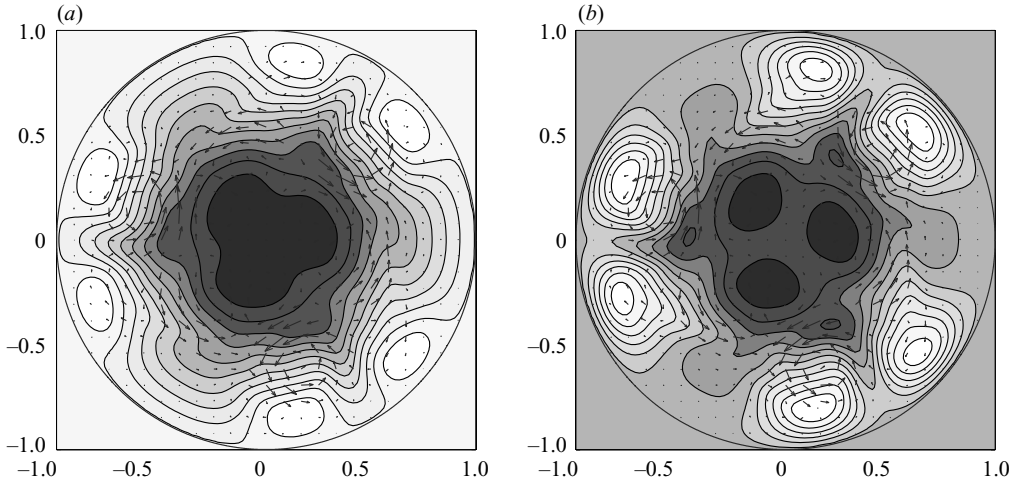

FIGURE 11. The structure of an $\mathscr{R}_3$ travelling wave on the solution branch corresponding to e at $\alpha = 2.44$, $c = 0.456$ and $Re_m = 3378$ (see figure 10) at a given pipe cross-section (truncation $(9, 26, 6)$). In (a), $\tilde{w}$ is contoured (constant Re) whereas in (b), contours are drawn for w_m (constant Re_m). In both plots, 12 contours are drawn between the maximum and minimum values of $\tilde{w}$ $(-0.47, 0.089)$ and w_m $(-0.17, 0.19)$. The three slow streaks near the pipe axis are shown particularly well in (b). As elsewhere, the shading(colour) outside the pipe corresponds to the zero level.

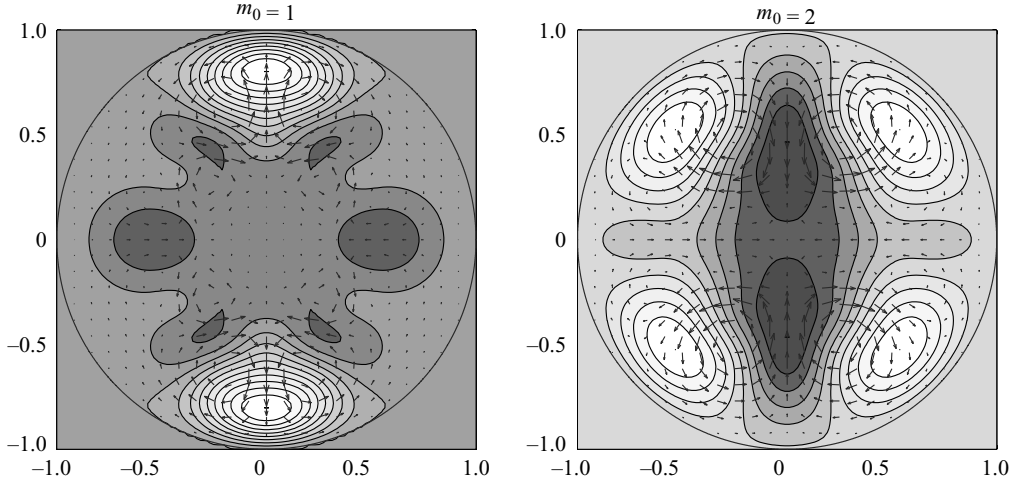

FIGURE 12. $\mathscr{R}_1$ and $\mathscr{R}_2$ travelling waves at their saddle-node bifurcation points and optimal wavenumber. The arrows indicate the streamwise-averaged cross-stream velocities $\overline{\boldsymbol{v}_\perp}^z = \overline{\tilde{u}}^z \hat{\boldsymbol{s}} + \overline{\tilde{v}}^z \hat{\boldsymbol{\phi}}$ (larger arrows corresponding to larger speeds) and the shading represents the streamwise-averaged axial velocity differential $\overline{w_m}^z$ (dark most negative and light most positive; the shading of the area exterior to the pipe represents zero). Ten contours are drawn between the maximum and minimum values of $\overline{w_m}^z$ as listed in table 2. Streamwise-averaging highlights the structure of the waves most clearly.

and select a new instability or adjust α. By far the most effective of these was to vary α, to which the feedback seemed very sensitive.

Figures 4 and 5 show the result of carrying out this procedure for the SSP solutions at $(m_0, \alpha, Re) = (2, 1.55, 2100)$ and $(m_0, \alpha, Re) = (3, 2.44, 1800)$ discussed above. The

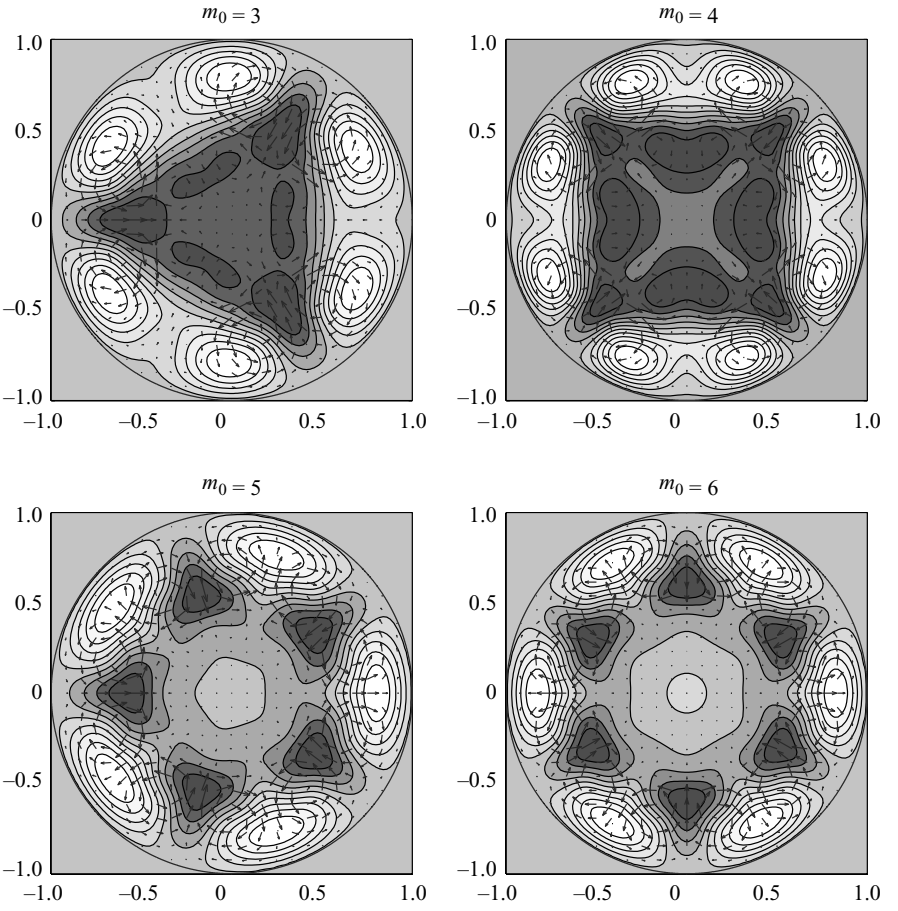

FIGURE 13. $\mathscr{R}_{m_0}$ travelling waves for $m_0 = 3, 4, 5, 6$ at their saddle-node bifurcation points and optimal wavenumber. The arrows indicate the streamwise-averaged cross-stream velocities $\overline{\boldsymbol{v}_\perp}^z = \overline{\widetilde{u}}^z \widehat{\boldsymbol{s}} + \overline{\widetilde{v}}^z \widehat{\boldsymbol{\phi}}$ (larger arrows corresponding to larger speeds) and the shading represents the streamwise-averaged axial velocity differential $\overline{w_m}^z$ (dark most negative and light most positive; the shading of the area exterior to the pipe represents zero). Ten contours are drawn between the maximum and minimum values of $\overline{w_m}^z$ as listed in table 2. Streamwise-averaging highlights the structure of the waves most clearly.

measure

$$\text{3D amp} := \sqrt{\sum_{n=0}^{N-1} |u_{n11}|^2 + |v_{n11}|^2 + |w_{n11}|^2} \tag{5.1}$$

plotted on the (left) y-axis is used to indicate the degree of three-dimensionality of the solution. In each figure, the two curves shown represent the data from one run of the branch tracing process at a representative truncation level. All the individual convergences of the root-finding algorithm are displayed (joined by straight lines to guide the eye) to indicate the relative ease (measured in terms of number of steps taken) with which the solution branch can be continued back the $A = 0$ axis. The jaggedness seen in the plots arises through any of three different effects. First, and dominantly, there is the strobing of the true smooth curve since only a finite number of solutions are shown joined by straight lines. Secondly, the projection of a smooth

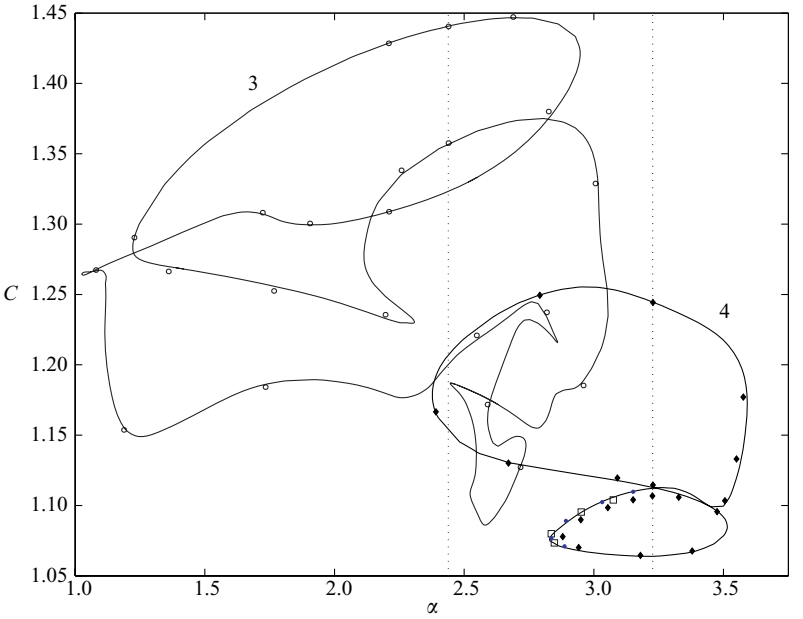

FIGURE 14. The phase speed normalized by the average streamwise speed $C = c \times W/\overline{W}$ as a function of the axial wavenumber α for $\mathscr{R}_3$- (labelled 3) and $\mathscr{R}_4$- (labelled 4) waves keeping $Re_m = 2000$. The truncations used to generate the two closed curves were (8, 28, 6) for $\mathscr{R}_3$ and (7, 35, 5) for $\mathscr{R}_4$. The curves were regularly checked for numerical convergence by, in the case of $\mathscr{R}_3$, using a (8, 28, 6) solution on the curve as a starting guess for the branch tracing code with (9, 24, 6) truncation. The resulting (9, 24, 6) solution was then plotted alongside the (8, 28, 6) curve using an open circle. The solid diamonds indicate the result of doing this for $\mathscr{R}_4$ using the truncation (6, 32, 6). Further checks were done for the lower $\mathscr{R}_4$ loop (dots are (7, 38, 5) and squares (7, 32, 6)). The vertical dotted lines are drawn at the optimal α^* values; $\alpha_3^* = 2.44$, $\alpha_4^* = 3.23$. Starting from the uppermost and in descending order, the crossings of $\alpha = 2.44$ by the $\mathscr{R}_3$ curve coincide with the solution branches in figure 10 corresponding to solutions d, a, e and f (the cusp near (2.45, 1.18) fails to cross the line $\alpha = 2.44$). This plot shows that the two branches confirmed in figure 10 are part of one convoluted $\mathscr{R}_3$ solution surface. It also shows that there are two solution branches for $\mathscr{R}_4$ at the optimal α (the lower loop is clearly more difficult to resolve numerically than the upper loop).

curve in higher dimensions onto the $A-3$D amp plane can cause apparent jerkiness and thirdly, the use of an insufficient truncation level can lead to sharp changes in the solution curve (the last effect is considered in more detail later). For the truncation level chosen, the path back to the unforced pipe flow situation ($A = 0$) in figure 4 ($m_0 = 2$) is direct and there are the expected two crossings corresponding to an upper and lower branch. Figure 5 ($m_0 = 3$), however, shows an indirect connection back to the $A = 0$ axis, hinting at the possibility of more convoluted behaviour. This is confirmed in figure 6 by considering the same SSP solution $(m_0, \alpha) = (3, 2.44)$ but further away from the saddle-node bifurcation at $Re = 2200$. After the initial smooth path back, the solution curve knits around the $A = 0$ axis crossing six times implying three separate upper and lower branch pairings. If these six solutions (along with the two for $m_0 = 2$) are used as starting points for branch continuation, the curves traced out are as in figure 7. This confirms that there is one solution branch for $m_0 = 2$ at truncation $(M, N, L) = (8, 25, 5)$ and $\alpha = 1.55$ (corroborated by higher truncations) and three separate branches for $m_0 = 3$ at $(M, N, L) = (8, 24, 5)$ and $\alpha = 2.44$ (partially

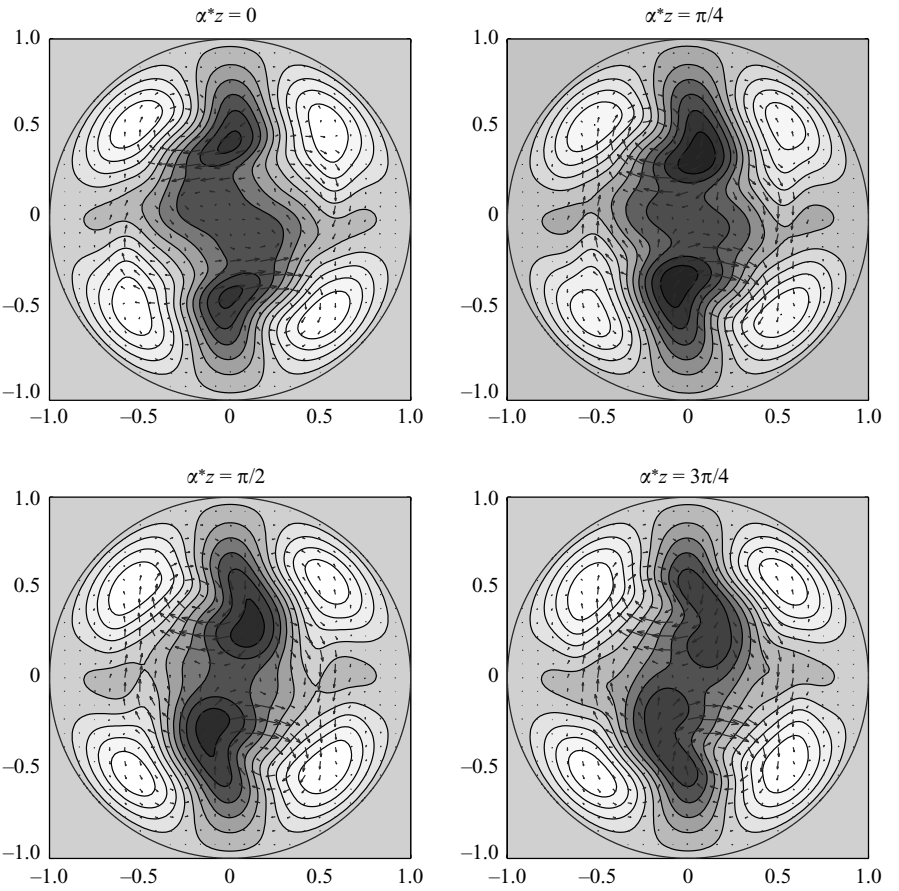

FIGURE 15. The $\mathscr{R}_2$ travelling wave solution at the saddle-node bifurcation $\alpha^* = 1.55$ and $Re = 1358.5$. The plots are cross-sections of the pipe with $\alpha^* z = 0, \pi/4, \pi/2, 3\pi/4$ (i.e. separated by $\pi/(4\alpha^*)$ along the axis). The cross-sections at $\alpha^* z = \pi, 5\pi/4, 3\pi/2, 7\pi/4$ are obtainable via the shift-and-reflect symmetry $\mathscr{S}_2$. The arrows indicate the cross-stream velocities $\boldsymbol{v}_\perp$ (larger arrows corresponding to larger speeds) and the shading represents the axial velocity w_m (dark most negative and light most positive, 12 contour levels used ranging from -0.2 and 0.2). Notice that the slow interior streaks move around whereas the fast outer streaks are effectively stationary.

confirmed by higher truncations; see below). The $m_0 = 3$ branch which reaches the lowest Re value of 1617 is the only branch existing at $Re = 1800$ (see figure 5) and achieves the smallest $Re_m = 1251$ (at $Re = 1631$).

The most notable difference in the structure of the multiple $m_0 = 3$ solutions is the number of fast streaks near the wall. Figure 8 shows streamwise-averaged plots of the total cross-stream velocity, $\boldsymbol{v}_\perp := \tilde{u}\hat{\boldsymbol{s}} + \tilde{v}\hat{\boldsymbol{\phi}}$, and the surplus streamwise speed $\tilde{w}$ for solutions a–f as marked on figures 6 and 7. Streamwise-averaging the velocity field brings into sharp focus the direct link between the streaks and the cross-stream flow which is arranged into a series of coherent rolls. Plotting contours of $\tilde{w}$ emphasizes the differences in the axial velocity of the travelling wave from that of the laminar solution which corresponds to the same applied pressure gradient or equivalently the same Re. From figure 6 (and the dashed A–c curve), the first crossing of $A = 0$ corresponds to solution a which has $m_0 = 3$ fast streaks near the wall. Not unexpectedly, this is

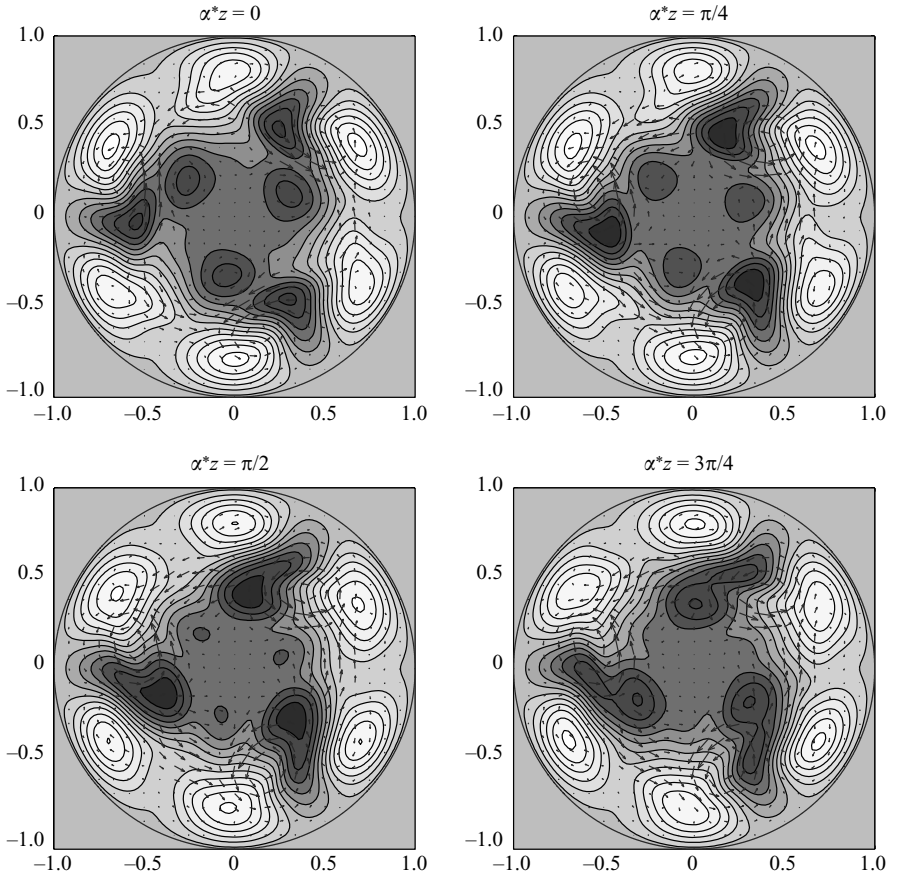

FIGURE 16. As figure 15 but for the $\mathscr{R}_3$ travelling wave solution at the saddle-node bifurcation $\alpha^* = 2.44$ and $Re = 1250.9$. The 12 contour levels used range from -0.15 to 0.15). Notice that the slow interior streaks move around whereas the fast outer streaks are fairly stationary.

very similar to the starting SSP roll + streak ansatz at the initial bifurcation point $(A, \text{3D amp}) = (A_{crit}, 0)$ displayed in figure 1. The next crossing at solution b also has m_0 fast streaks while at the third crossing, solution c seems in transition between m_0 and $2m_0$ fast streaks. Subsequent crossings at d, e and f all yield solutions with $2m_0$ fast streaks.

Fast streaks occur where there is a cross-stream velocity directed to the pipe wall and slow streaks occur when there is a cross-stream velocity away from the wall. The transition from m_0 to $2m_0$ fast streaks seems to coincide with the spatial broadening of the m_0 cross-stream outflows. In contrast, the cross-stream inflows always stay focused but can have significant axial variation. This appears to make the slow streaks more variable in structure and positioning than the outer fast streaks which are very two-dimensional. Figure 9 illustrates this by contrasting solutions a and f. Here, instead of using $\tilde{w}$,

$$w_m := \tilde{w} + (1 - Re_m/Re)(1 - s^2) \tag{5.2}$$

is contoured which corresponds to the difference of the travelling wave axial velocity from a laminar state with the same mass flux or Re_m and particularly highlights the slow streak structure in the interior. Comparing the velocity field at an arbitrary axial

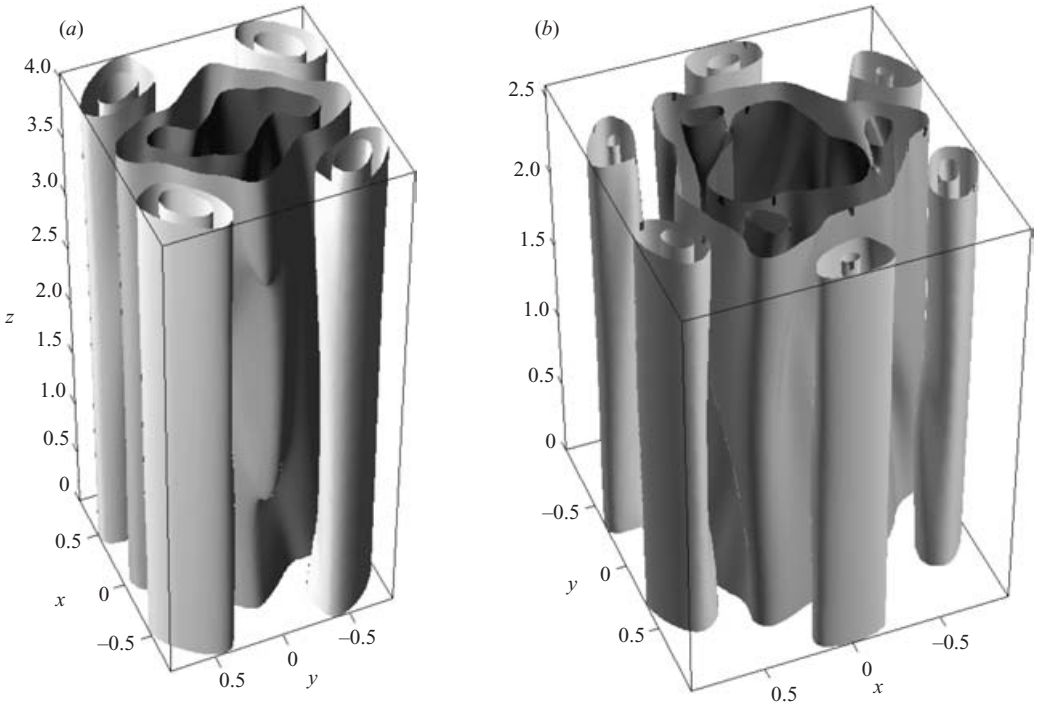

FIGURE 17. Isosurfaces of the axial velocity differential $\tilde{w}$ for $\mathscr{R}_2$ (a) and $\mathscr{R}_3$ (b) travelling waves at their saddle-node bifurcations and optimal wavenumbers. The pipe axis is directed bottom to top and runs from $z=0$ to $z=2\pi/\alpha^*$; x and y are Cartesian coordinates across the pipe section of radius 1 centred on $(x, y)=(0, 0)$. The outer light contours indicate fast streaks and the inner dark slow streaks. (Four contours are drawn at -0.028, -0.015, 0.01 and 0.05 in each plot.) Again notice that the outer fast streaks are almost two-dimensional.

cross-section with a streamwise-averaged version shows little variation for solution a where there are m_0 fairly two-dimensional slow streaks. In contrast, solution f has $2m_0$ interior slow streaks with significant three-dimensional variation so that their streamwise average becomes almost featureless in the interior.

All these solutions except for the 'transitional' solution c can be confirmed using increased truncation levels. Figure 10 shows the results of following the branches using a variety of larger truncations. (A branch section is inferred to exist and is drawn with a solid or dashed line if a variety of truncations traced it out successfully.) The presence of multiple branches on this slice ($\alpha=2.44$) of the $m_0=3$ solution surface is confirmed although two branches appear (see the (9, 26, 6) results in figure 10) rather than the three suggested in figure 7 by the lower truncation of (8, 24, 5) (which still represents over 10 000 degrees of freedom). The structure of the flow solutions on the branches which extend to higher Re_m (>2600) closely resembles the corresponding solution structure illustrated in figure 8. For example, on the lowest branch, which passes through solution f, the travelling wave at $Re_m=2600$ has $2m_0$ fast streaks equispaced around the pipe perimeter just like f. The one notable exception to this observation is provided by the branch corresponding to solution e. Here there are $2m_0$ fast streaks as for solution e but they not equally spaced around the pipe perimeter, appearing ready to merge in pairs. Figure 11 shows both $\tilde{w}$ and $\tilde{w}+(1-Re_m/Re)(1-s^2)$ contoured for this solution at one cross-section of the pipe. The constant-mass plot on the right shows the presence of $m_0=3$ dominant

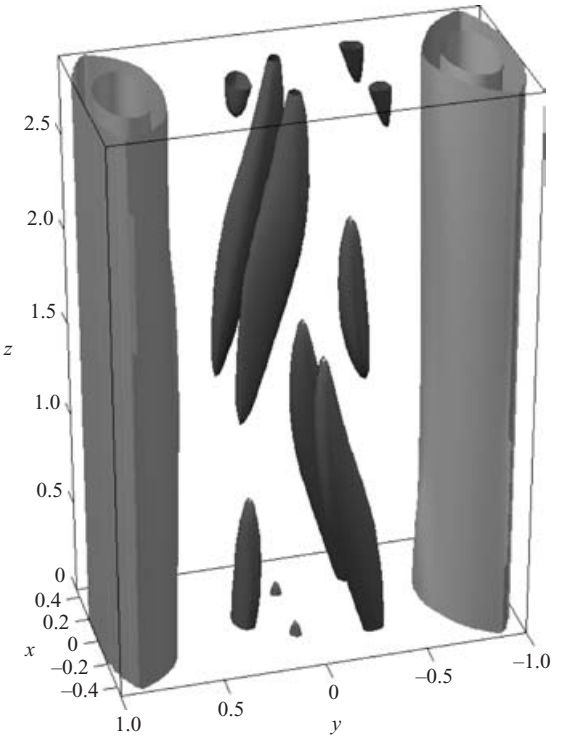

FIGURE 18. Isosurfaces of axial velocity differential $\tilde{w}$ for the $\mathscr{R}_1$-wave at its saddle-node bifurcation and optimal wavenumber. The pipe axis is directed bottom to top and runs from $z=0$ to $z=2\pi/\alpha_1^*$; x and y are Cartesian coordinates across the pipe section of radius 1 centred on $(x, y)=(0, 0)$. The outer light contours at 0 and 0.1 indicate the two fast streaks which are very close to the wall at $(x, y)=(0, \pm 1)$ and the inner darker contour at -0.255 shows the slow streaks. Only three contour levels have been chosen to illustrate that the fast outer streaks have dominantly $\mathscr{R}_2$ symmetry but the slow inner streaks clearly only have $\mathscr{R}_1$.

slow streaks in the interior indicating that there is no simple connection between the number of fast streaks and slow streaks (see also the $\mathscr{R}_2$-wave in figure 12).

5.2. *Travelling wave solutions*

The objective once a travelling wave solution had been found was to map out the solution surface as much as was practical until

$$\min_{Re,\alpha} Re_m(m_0)$$

was found. Given the multiple solution branches already found for $m_0=3$, this is a daunting numerical undertaking. As a result, we have contented ourselves here with getting onto *a* solution surface for each m_0 value up to 6 using the SSP analysis to guide our starting point and then searching smoothly around on this for $\min_{Re,\alpha} Re_m(m_0)$. So, given this uncertainty in the solution surface topology, we can say only that $\mathscr{R}_{m_0}$-waves certainly exist down to some value of Re_m rather than the stronger (and preferable) statement that $\mathscr{R}_{m_0}$-waves only appear for Re_m above some threshold value. To emphasize this, figures 12 and 13 indicate that we have found $2m_0$-streak solutions for $m_0=2, 3, 4$ at the respective saddle-node bifurcation but only m_0-streak solutions for $m=5, 6$. Whether corresponding solutions of the other type

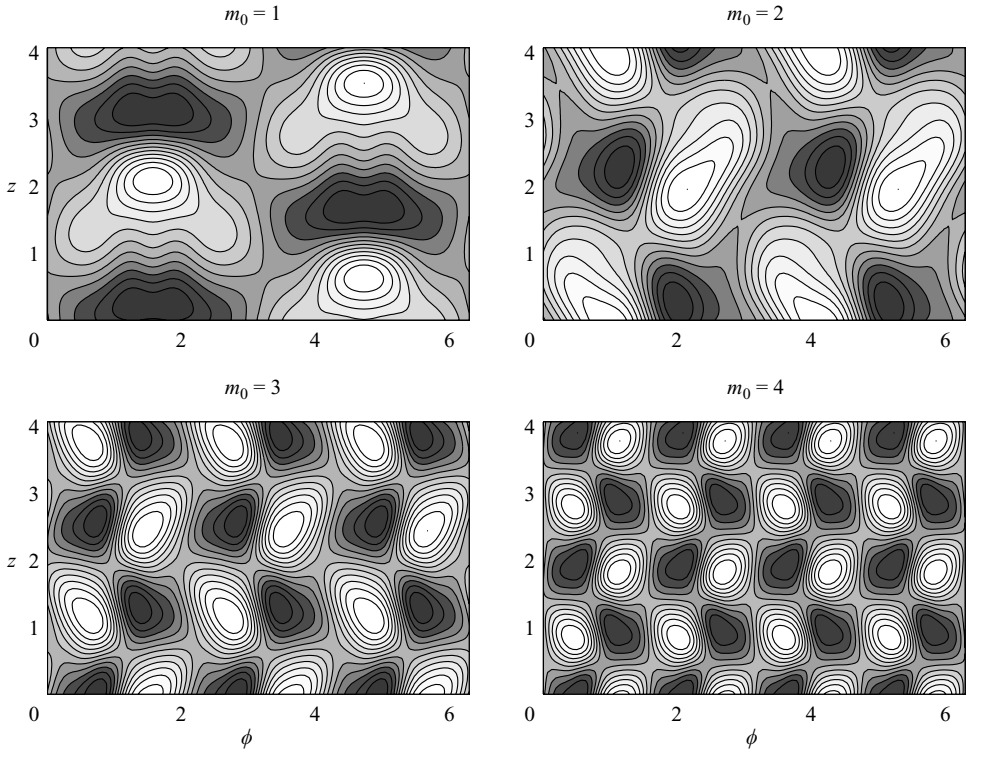

FIGURE 19. The pressure field at the pipe wall $s = 1$ associated with the $\mathscr{R}_{m_0}$ travelling waves at their minimum Re_m values (and hence optimal $\alpha = \alpha^*$). For ease of comparison, the pressure fields are contoured over $0 \leqslant \phi \leqslant 2\pi$ and $0 \leqslant z \leqslant 2\pi/\alpha_2^*$ where $\alpha_2^* = 1.55$ is the smallest optimal wavenumber over $m_0 = 1$ to 6 and so corresponds to the longest wavelength. Equally spaced contours are drawn ranging from the pressure minimum p_{min} to the pressure maximum p_{max} (12 drawn for $m_0 = 1, 2, 3$ and 10 for $m_0 = 4$) and dark corresponds to negative values whereas light to positive values. $(p_{min}, p_{max}) = (-3.0, 3.8) \times 10^{-4}$ for $\mathscr{R}_1$, $(-5.0, 4.6) \times 10^{-4}$ for $\mathscr{R}_2$, $(-7.9, 7.8) \times 10^{-4}$ for $\mathscr{R}_3$ and $(-6.2, 7.6) \times 10^{-4}$ for $\mathscr{R}_4$.

exist at lower Re_m remains uncertain. Faisst & Eckhardt (2003) do report finding a $2m_0$-streak solution for $m_0 = 5$ but admit that it is not properly resolved.

Figure 14 hints at the complexity of the situation. Here two known $\mathscr{R}_3$ and $\mathscr{R}_4$ solutions at $Re_m = 2000$ were used as starting points to trace out their respective solution surface cross-sections defined by $Re_m = 2000$. The initial motivation for this was to assess the range of α and $C = cW/\overline{W}$ (the phase speed normalized by the average streamwise speed) over which the travelling waves exist at this experimentally relevant Re_m. While these data certainly emerge – $1.0 < \alpha < 3.1$ and $1.09 < C < 1.45$ for $\mathscr{R}_3$, and $2.38 < \alpha < 3.6$ and $1.06 < C < 1.26$ for $\mathscr{R}_4$ – the more striking information revealed is how the two $\mathscr{R}_3$ solution branches already found are smoothly connected and the discovery of two $\mathscr{R}_4$ solution branches at $\alpha = \alpha_4^* = 3.23$. The four crossings of the optimal wavenumber $\alpha = 2.44$ line by the $\mathscr{R}_3$ curve coincide with the branches shown in figure 10: starting from the highest C value and in descending order, the intersections are by the branches corresponding to solutions d, a, e and f. Both loops of the $\mathscr{R}_4$-wave solutions have $2m_0$ streaks with the upper (in C) larger (and better converged) loop leading to a lowest Re_m value of 1647 (see table 2 below).

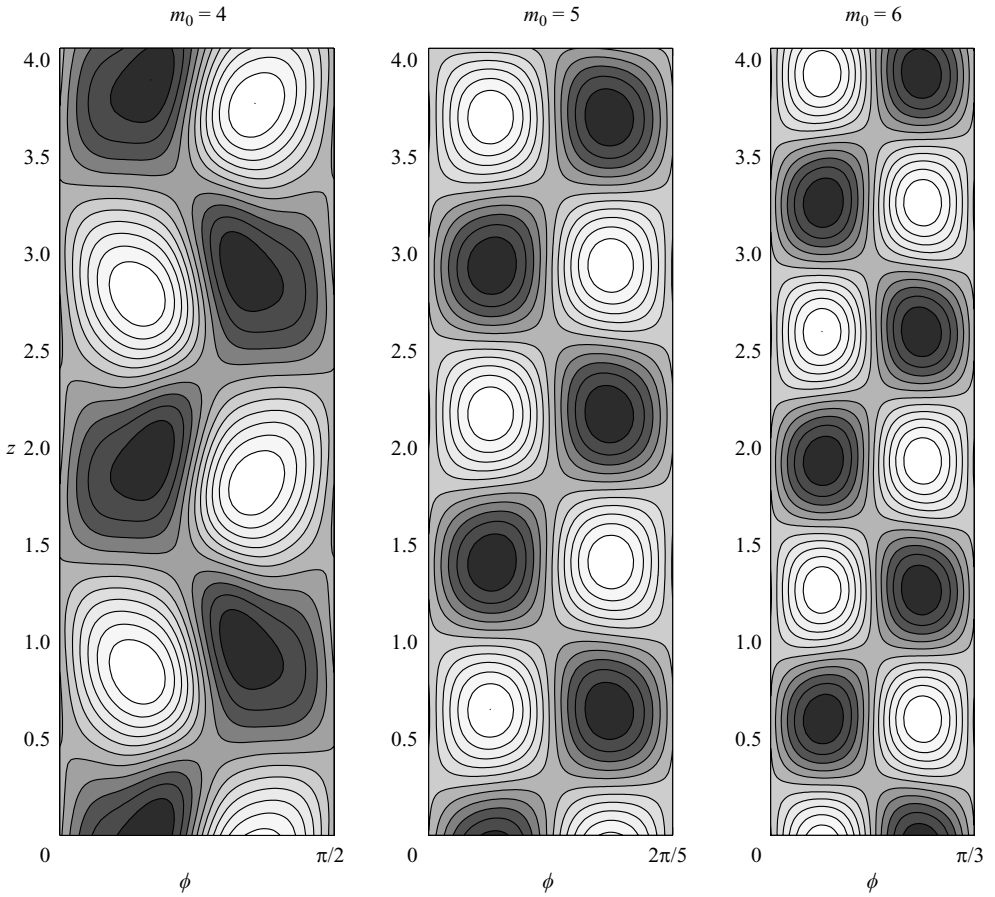

FIGURE 20. The pressure field at the pipe wall $s = 1$ associated with the $\mathscr{R}_{m_0}$ ($m_0 = 4, 5, 6$) travelling waves at their minimum Re_m values (and hence optimal $\alpha = \alpha^*$). As in figure 19, contours are drawn over $0 \leqslant z \leqslant 2\pi/\alpha_2^*$ but for clarity, ϕ is now restricted to $[0, 2\pi/m_0]$. The $\mathscr{R}_4$ pressure field is reproduced here for comparison purposes. As in figure 19, 12 contours are drawn at equal intervals ranging from the minimum pressure p_{min} to the maximum pressure p_{max}: $(p_{min}, p_{max}) = (-6.2, 7.6) \times 10^{-4}$ for $\mathscr{R}_4$, $(-3.2, 3.3) \times 10^{-4}$ for $\mathscr{R}_5$ and $(-2.7, 2.8) \times 10^{-4}$ for $\mathscr{R}_6$.

The structural difference in the streamwise-averaged velocity fields shown in figures 12 and 13 between the $2m_0$ fast streak $\mathscr{R}_2$, $\mathscr{R}_3$ and $\mathscr{R}_4$ solutions and the m_0 fast streak $\mathscr{R}_5$ and $\mathscr{R}_6$ solutions also reveals itself in the three-dimensionality of the slow interior streaks. The slow streaks move around and modulate in amplitude along the pipe in the $\mathscr{R}_2$- (see figure 15), $\mathscr{R}_3$- (see figure 16) and $\mathscr{R}_4$-waves whereas the slow streaks are fairly stationary and hence two-dimensional for the $\mathscr{R}_5$ and $\mathscr{R}_6$ solutions. In contrast, for all waves found the fast outer streaks are essentially two-dimensional. A three-dimensional visualization shown in figure 17 of the axial variation of the travelling $\mathscr{R}_2$- and $\mathscr{R}_3$-waves reiterates this, showing how the inner slow streaks meander around whereas the outer fast streaks are surprisingly stationary and hence two-dimensional. Figure 18 shows three isosurfaces of axial velocity differential $\tilde{w}$ for the $\mathscr{R}_1$-wave (at its saddle-node bifurcation and optimal wavenumber) which capture the fast and slow streak structure. This illustrates that the fast outer streaks have dominantly $\mathscr{R}_2$

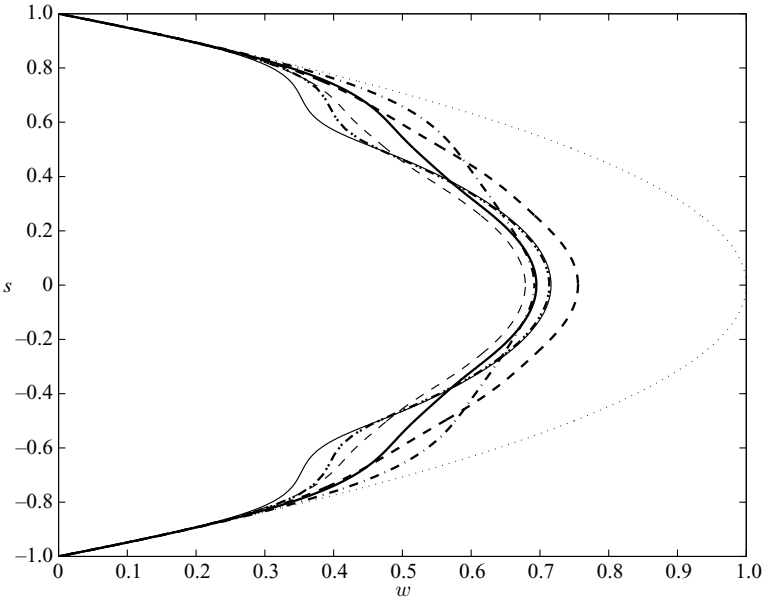

FIGURE 21. The mean axial velocity profile for the $\mathscr{R}_{m_0}$ ($m_0 = 1, \ldots, 6$) travelling waves at their saddle-node points and (hence optimal wavenumbers). The profiles are compared to the equivalent laminar profile (dotted line) at the same applied pressure gradient (i.e. same Re). The axial velocity corresponding to $\mathscr{R}_1$ is the thick grey dashed line, $\mathscr{R}_2$ is the black dash-dot line, $\mathscr{R}_3$ is the thick solid line, $\mathscr{R}_4$ is the thin grey dashed line, $\mathscr{R}_5$ is the thick dash-dot line and $\mathscr{R}_6$ is the thin solid line. Going from right to left along the radius $s = 0.6$, the curves correspond to the laminar state $1 - s^2$, $\mathscr{R}_2$, $\mathscr{R}_1$, $\mathscr{R}_3$, $\mathscr{R}_4$, $\mathscr{R}_5$ and finally $\mathscr{R}_6$.

symmetry and are fairly two-dimensional whereas the slow inner streaks clearly only have $\mathscr{R}_1$ symmetry and vary in the axial direction.

The pressure distribution on the pipe wall appears to be a robust indicator of the rotational symmetry of the $\mathscr{R}_{m_0}$-wave. Figures 19 and 20 show contour plots of the pressure distribution on the pipe wall for the $\mathscr{R}_{m_0}$ solutions at their respective saddle-node bifurcations. The number of pressure peaks around a pipe circumference is exactly m_0 regardless of whether there are m_0 or $2m_0$ fast streaks. This is because the pressure field is decoupled from the streamwise-independent axial flow structures. As way of confirmation, the pressure fields associated with the various $m_0 = 3$ solutions a, b, d, e and f produce similar plots to that shown in figure 19 albeit the individual cells vary in exact shape somewhat. Furthermore, the $\mathscr{R}_1$-wave has two fast streaks but only one pressure maximum around the boundary at a given station z along the pipe. The range of the pressure values at the wall (in non-dimensional units of ρW^2) is largest for $\mathscr{R}_3$ at $(p_{min}, p_{max}) = (-7.9, 7.8) \times 10^{-4}$ corresponding to the lowest Re_m value of 1251, and smallest for $\mathscr{R}_6$ where $(p_{min}, p_{max}) = (-2.7, 2.8) \times 10^{-4}$ and Re_m is largest at 2869 (excepting the $\mathscr{R}_1$-wave which has a different structure).

The mean (azimuthally and streamwise) axial velocities of the travelling waves at their saddle-node bifurcation points are shown compared to the equivalent laminar flow at the same pressure gradient (i.e. Re) in figure 21 and at the same mass flux (i.e. Re_m) in figure 22. Figure 21 shows that all the profiles possess a change in the shear or a 'shoulder' at a radius of between 0.6 and 0.8 which is approximately where the fast streaks reach from the pipe wall (except $\mathscr{R}_1$ which has a different structure). At this radius the profiles are arranged in strict order ($m_0 = 2$ to 6); however, at the pipe

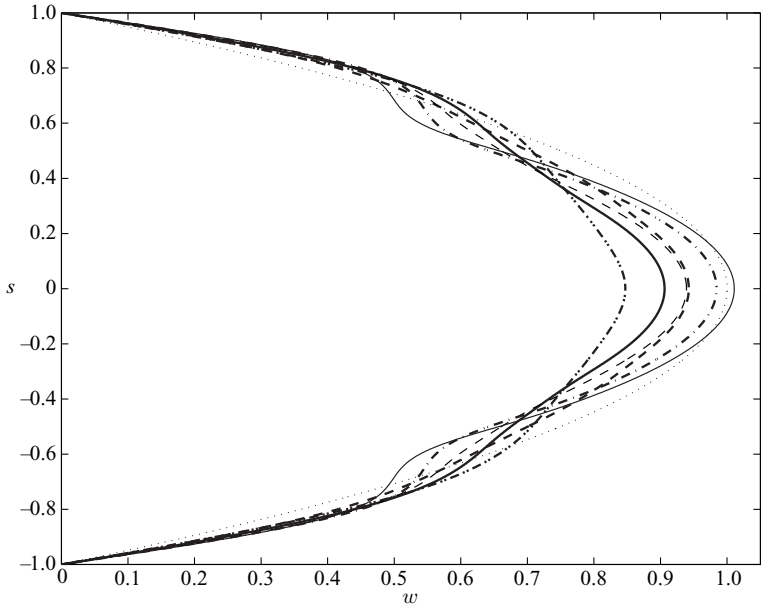

FIGURE 22. As in figure 21 but now comparing the mean axial velocity profile for the travelling waves with a laminar profile (dotted line) corresponding to the same mass flux (i.e. same Re_m). The axial velocity corresponding to $\mathscr{R}_1$ is the thick grey dashed line, $\mathscr{R}_2$ is the thin black dash-dot line, $\mathscr{R}_3$ is the thick solid line, $\mathscr{R}_4$ is the thin dashed line, $\mathscr{R}_5$ is the thick grey dash-dot line and $\mathscr{R}_6$ is the thin solid line. Going from right to left along the axis $s=0$, the curves correspond to $\mathscr{R}_6$, the laminar state $1-s^2$, $\mathscr{R}_5$, $\mathscr{R}_1$, $\mathscr{R}_4$, $\mathscr{R}_3$ and $\mathscr{R}_2$.

	$\mathscr{R}_1$	$\mathscr{R}_2$	$\mathscr{R}_3$	$\mathscr{R}_4$	$\mathscr{R}_5$	$\mathscr{R}_6$
$\min_\alpha Re_m$	3046	1358.5	1250.9	1647	2485.5	2869
α^*	2.17	1.55	2.44	3.23	4.11	4.73
$C(=cW/\overline{W})$	1.56	1.44	1.28	1.16	1.08	1.00
Corresponding Re	3800	1663	1631	2280	3427	4069
Estimated error in Re_m	± 10	± 0.5	± 0.5	± 3	± 0.5	± 2
Truncation	(9, 36, 5)	(8, 30, 8)	(9, 35, 6)	(7, 35, 6)	(7, 35, 7)	(7, 40, 5)
Degrees of freedom	16200	19260	19390	15470	17710	15120
$\overline{W}/W$	0.401	0.408	0.384	0.362	0.363	0.353
max $\overline{\tilde{w}}^z$	0.21	0.076	0.057	0.048	0.064	0.060
min $\overline{\tilde{w}}^z$	−0.25	−0.32	−0.31	−0.33	−0.33	−0.32
max $\overline{w_m}^z$	0.28	0.15	0.14	0.13	0.15	0.14
min $\overline{w_m}^z$	−0.09	−0.16	−0.11	−0.09	−0.14	−0.13
max$\lvert\overline{\boldsymbol{v}_\perp}^z\rvert$	0.0091	0.014	0.018	0.020	0.0092	0.0087

TABLE 2. Optimal properties of the travelling wave solutions at their saddle-node bifurcation points. The value of Re corresponding to min Re_m is given although this is not the minimum value of this parameter, only close to it. The velocity measures quoted at the bottom ($\boldsymbol{v}_\perp = \tilde{u}\hat{\boldsymbol{s}} + \tilde{v}\hat{\boldsymbol{\phi}}$ is the cross-stream velocity) of the table are measured on the z-averaged velocity field so as to illustrate the difference in scale between the streamwise rolls and the streaks (in units of the laminar centreline speed W).

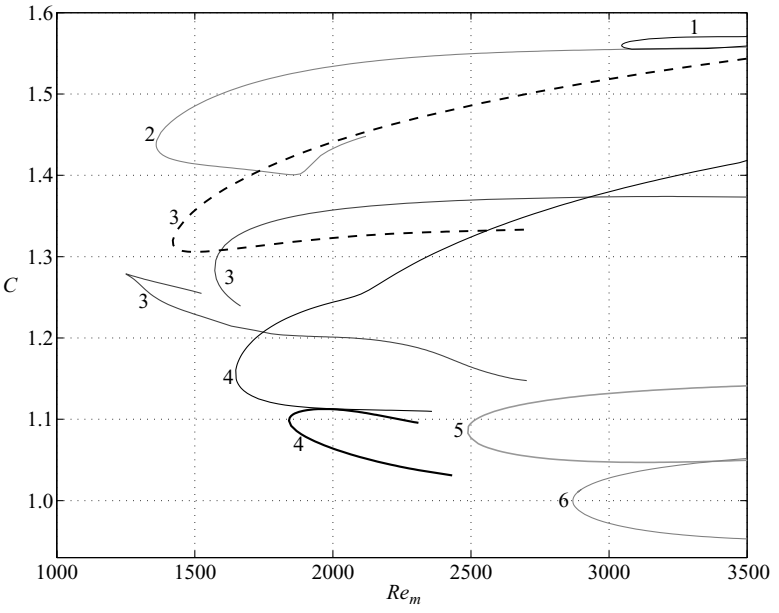

FIGURE 23. The phase speed normalized by the average streamwise speed, $C = c \times W/\overline{W}$ as a function of Re_m for the different m_0 solution branches at their optimal wavenumber α^*. Each branch is shown only as far as it is assured to be resolved, i.e. different truncations produce overlapping curves. Truncations used to check this were: (9, 35, 5) and (9, 36, 5) for $m_0 = 1$, (8, 25, 5) & (9, 27, 6) for $m_0 = 2$, (8, 24, 5), (8, 24, 7), (9, 28, 5), (8, 28, 6) and (9, 26, 6) for the multiple branches of $m_0 = 3$, (6, 32, 6) and (7, 35, 5) for the two branches of $m_0 = 4$, (7, 32, 4) and (7, 35, 5) for $m_0 = 5$, (7, 32, 4) and (7, 40, 5) for $m_0 = 6$. The branches are as follows in descending order from top of the graph: the $\mathscr{R}_1$ subharmonic ($Re_m > 3000$), $\mathscr{R}_2$, $\mathscr{R}_3$, $\mathscr{R}_4$, $\mathscr{R}_5$ and $\mathscr{R}_6$ respectively. The dashed $\mathscr{R}_3$ solution branch corresponds to the dashed solution branches in figures 7 and 10 and the thick line represents the lower loop of $\mathscr{R}_4$ solutions in figure 14. The phase speed systematically decreases with increasing m_0.

axis this ordering is destroyed with $\mathscr{R}_4$ having a smaller centreline speed compared to $\mathscr{R}_2$ and $\mathscr{R}_3$ whereas $\mathscr{R}_5$ and $\mathscr{R}_6$ have larger centreline speeds. This could be another signature of the change in structure which occurs between the $\mathscr{R}_4$- and $\mathscr{R}_5$-waves although since these profiles are being compared at different Re this is a little unclear. Figure 22 shows the same ordering in the shoulder feature and precisely the reversed ordering at the pipe axis with the $\mathscr{R}_6$-wave having a larger speed than the laminar flow there. This perfect reordering is essentially forced as all the waves have nearly the same gradient at the pipe wall and the profiles must carry the same mass flux down the pipe (the volume of revolution of the curves around $s = 0$ must be equal).

Table 2 brings together information about the travelling waves at the lowest Re_m where they were detected, that is, at the saddle-node bifurcation point for the optimal wavenumber α^*. A number of systematic trends appear as m_0 increases. First, the critical Re_m value grows, presumably because the fast streaks are pushed towards the pipe wall and hence suffer enhanced dissipation. The optimal wavenumber α^* increases in sympathy with the smaller streak scales generated near the wall. The waves also become slower and the mean velocity decreases. The structural differences in the waves are also apparent from the simple velocity measures shown too. $\mathscr{R}_1$-waves stand out by having fast streak $\tilde{w}$ velocities comparable to slow streak $\tilde{w}$ velocities whereas in all the other waves, the latter dominate the former. If, instead,

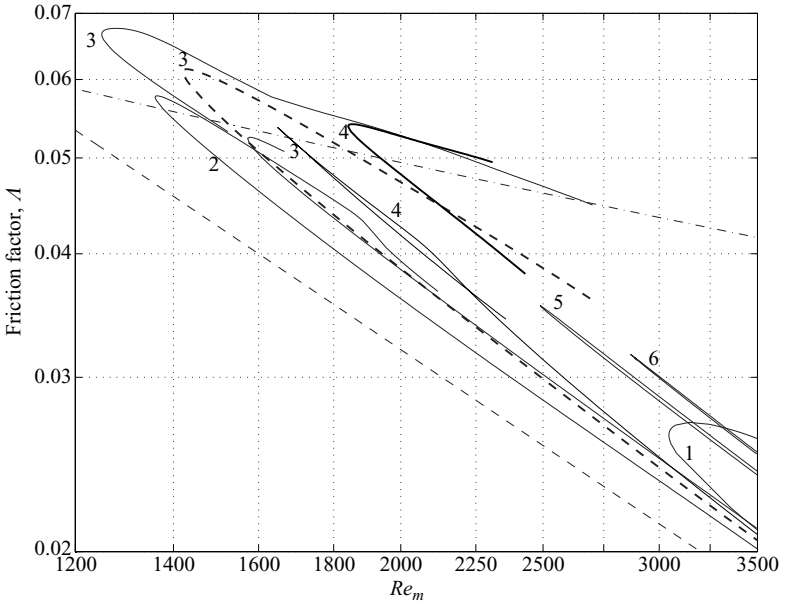

FIGURE 24. The friction factor $\Lambda := 64Re/Re_m^2$ for the travelling wave branches (labelled by m_0) at their optimal wavenumber α^*. The dashed straight line represents the lower bound given by the Hagen–Poiseuille solution ($\Lambda = 64/Re$) and the upper straight dash-dot line corresponds to the log-law parametrization of experimental data $1/\sqrt{\Lambda} = 2.0\log(Re_m\sqrt{\Lambda}) - 0.8$ (see Schlichting 1968, equation (20.30)). The thick dashed line corresponds to the $m_0 = 3$ dashed line in figures 7, 10 and 23. The solid thick line represents the lower loop of $m_0 = 4$ solutions shown in figure 14.

w_m is considered, the fast and slow streaks are essentially of equal magnitude for the modes except $\mathscr{R}_1$. The peak slow streak $\tilde{w}$ velocity is fairly uniform across all the fundamental waves but the $2m_0$ fast streak solutions ($\mathscr{R}_{m_0}$ $m_0 = 2, 3, 4$) have stronger cross-stream velocities than the m_0 fast streak solutions ($\mathscr{R}_{m_0}$ $m_0 = 5, 6$). In all cases, the streak velocities are typically an order of magnitude larger than the cross-stream velocities. The entries for $\mathscr{R}_2$ and $\mathscr{R}_3$ confirm and improve the results quoted by Faisst & Eckhardt (2003) since much higher truncation levels are used here.

Figure 23 shows the various travelling solution branches traced as far as they could be assured resolved by overlaying curves from different truncation runs. The systematic trend in the phase speed (decreasing as m_0 increases) is particularly apparent as are the respective positions of the critical $Re_m(m_0)$. The fact that the subharmonic $\mathscr{R}_1$-wave curve flanks the fundamental $\mathscr{R}_2$ curve suggests that pursuing subharmonic and other forms of $\mathscr{R}_m$ streak instability based on a $\mathscr{R}_{2m}$ roll + streak structure may always produce solutions with neighbouring curves similar to the fundamental $\mathscr{R}_{2m}$ curve. The dissipation rate associated with these $\mathscr{R}_{m_0}$-waves is compared in figure 24 to the Hagen–Poiseuille value and the experimental log-law parametrization of post-transition flows. Interestingly, the dissipation rates associated with $\mathscr{R}_2$-, $\mathscr{R}_3$- and $\mathscr{R}_4$-waves can exceed the log-law value, although only the $\mathscr{R}_3$ and $\mathscr{R}_4$ branches are able to do this at post-transitional Re_m. It is tempting to speculate that there may well be other $\mathscr{R}_5$- and $\mathscr{R}_6$-waves which also have such high friction factors yet to be found. An obvious strategy to explore this is to repeat the solution tracing exercise reported in figure 14 since this was how the dissipative $\mathscr{R}_4$-wave branch was discovered. Unfortunately, however, it is no coincidence that

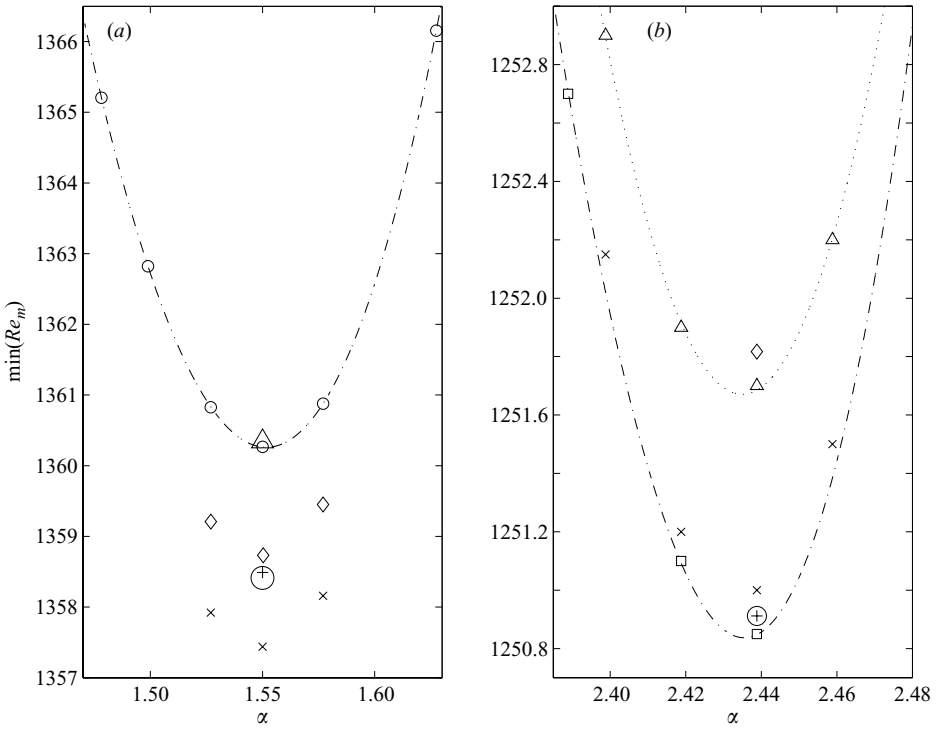

FIGURE 25. Dependence of the critical mean Reynolds number Re_m on the streamwise wavenumber α. (*a*) $\mathscr{R}_2$ travelling waves with truncations (M, N, L): ○ (8, 25, 5) (with a polynomial fit through), × (8, 25, 6), ◇ (8, 25, 7), ○ (8, 25, 9), △ (9, 25, 5), and + (8,30,8). All the truncations show the same optimal α to the grid resolution of 0.02 and good convergence once $M \geqslant 8$, $N \geqslant 25$ and $L \geqslant 7$. (*b*) $\mathscr{R}_3$ travelling waves with truncations: □ (8, 24, 5) (with polynomial fit), × (10, 24, 5), △ (9, 25, 6) (with polynomial fit), ◇ (9, 25, 7), ○ (9, 30, 6) and + (9, 35, 6). All the truncations show the same optimal α to the grid resolution of 0.02 and very good convergence once $M \geqslant 8$, $N \geqslant 24$ and $L \geqslant 5$.

the travelling wave solutions with the largest friction factors are also the hardest to resolve numerically. The solution branches which have been numerically resolved up to $Re_m = 3500$ all have the same (weak) asymptotic friction behaviour as the laminar Hagen–Poiseuille flow albeit with a larger numerical coefficient.

Figures 25, 26 and 27 indicate how the numerical values for Re_m quoted in table 2 are decided upon. Identifying $\min_{\alpha, Re} Re_m(m_0)$ is a painstaking task since the search is over a two-dimensional parameter space and the appropriate truncation level required for a given accuracy is unknown *a priori*. The strategy adopted was to use a moderately high truncation level to isolate the neighbourhood of the minimum before employing a suite of higher truncations to assess the likely accuracy given the inevitable hardware restrictions. For example, in the case of $\mathscr{R}_3$, the truncation $(M, N, L) = (8, 24, 5)$ proves adequate to locate α_3^* (checked by truncations (9, 25, 6) and (10, 24, 5)). Then higher resolutions such as (9, 25, 7), (9, 30, 6) and (9, 35, 6) were employed to refine the estimate of min Re_m. Figures 28 and 29 illustrate the spectral makeup of the $\mathscr{R}_3$ travelling wave at its saddle-node bifurcation point $Re = 1251$, which is the lowest of all waves found.

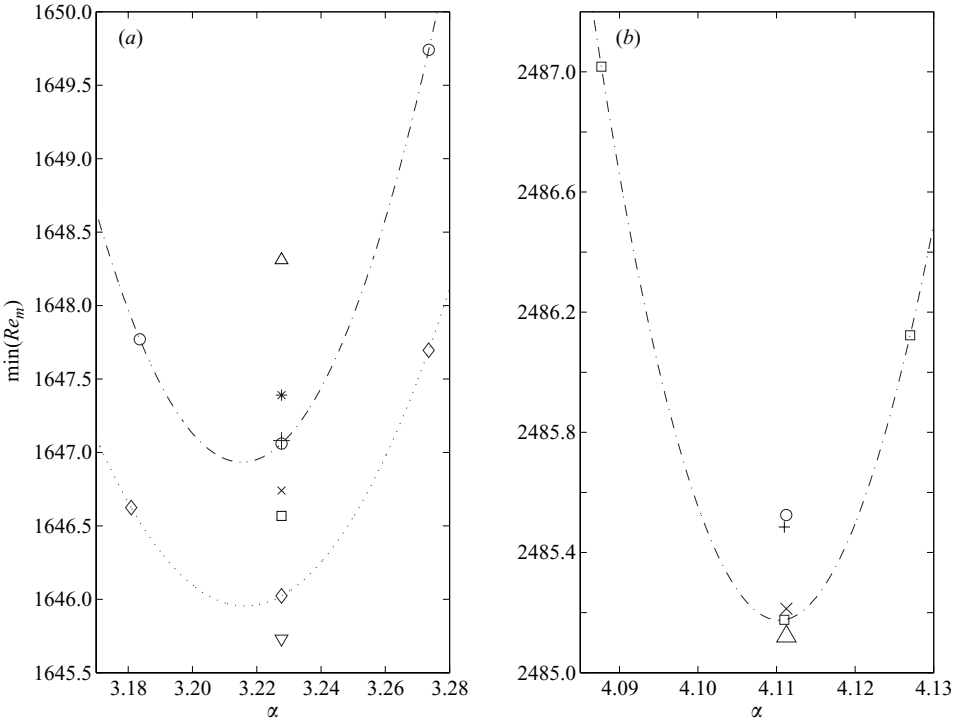

FIGURE 26. Dependence of the critical mean Reynolds number Re_m on the streamwise wavenumber α. (*a*) $\mathscr{R}_4$ travelling waves with truncations (M, N, L): $\diamond$ (6, 30, 5) (with dotted polynomial fit), $\circ$ (7, 35, 5) (with dash-dot polynomial fit), $\square$ (8, 35, 5), $\triangledown$ (6, 30, 6), $+$ (7, 40, 5), $\times$ (6, 35, 7), $\triangle$ (7, 35, 6), $*$ (6, 35, 6). The travelling wave $\mathscr{R}_4$ was the hardest to resolve numerically as indicated here; min(Re_m) can only be quoted with a ± 3 accuracy. In contrast, $\mathscr{R}_5$ was one of the easiest waves to resolve. (*b*) $\mathscr{R}_5$ travelling waves with truncations: $\square$ (7, 35, 5) (with polynomial fit), $\circ$ (7, 35, 6), $+$ (7, 35, 7), $\times$ (7, 40, 5) and $\triangle$ (8, 35, 5). Very good convergence is obtained for $M \geqslant 7$, $N \geqslant 35$ and $L \geqslant 6$.

6. Discussion

In this paper we have found three-dimensional travelling wave solutions for pressure-driven fluid flow through a circular pipe. These possess certain pre-selected symmetries (the shift-and-reflect symmetry $\mathscr{S}_2$ and a rotational symmetry $\mathscr{R}_{m_0}$ for some integer m_0) and have been constructed by mixing three key flow structures – two-dimensional streamwise rolls, streaks and three-dimensional streamwise-dependent waves – in the right way. *Fundamental* travelling waves (the solution shares the same rotational symmetry $\mathscr{R}_{m_0}$ as the component rolls and streaks) have been found for $m_0 = 2, 3, 4, 5, 6$. *Subharmonic* travelling waves (the component rolls and streaks are $\mathscr{R}_{2m_0}$ rotationally symmetric whereas the solution is only $\mathscr{R}_{m_0}$) have been found for $m_0 = 1$. All are born out of saddle-node bifurcations and presumably are unstable immediately – Faisst & Eckhardt (2003) find that the $m_0 = 2$ and the lowest branch of $m_0 = 3$ waves are unstable from the onset. The travelling waves which survive to the lowest value of the Reynolds number ($m_0 = 3$) appear to represent the best compromise between the confining cylindrical geometry offered by the pipe and the damping effects of the wall region. At small values of m_0, the rolls are large and centred away from the walls but, it seems, interact negatively inhibiting the establishment of a travelling wave. (The absence of an $m_0 = 1$ fundamental wave for

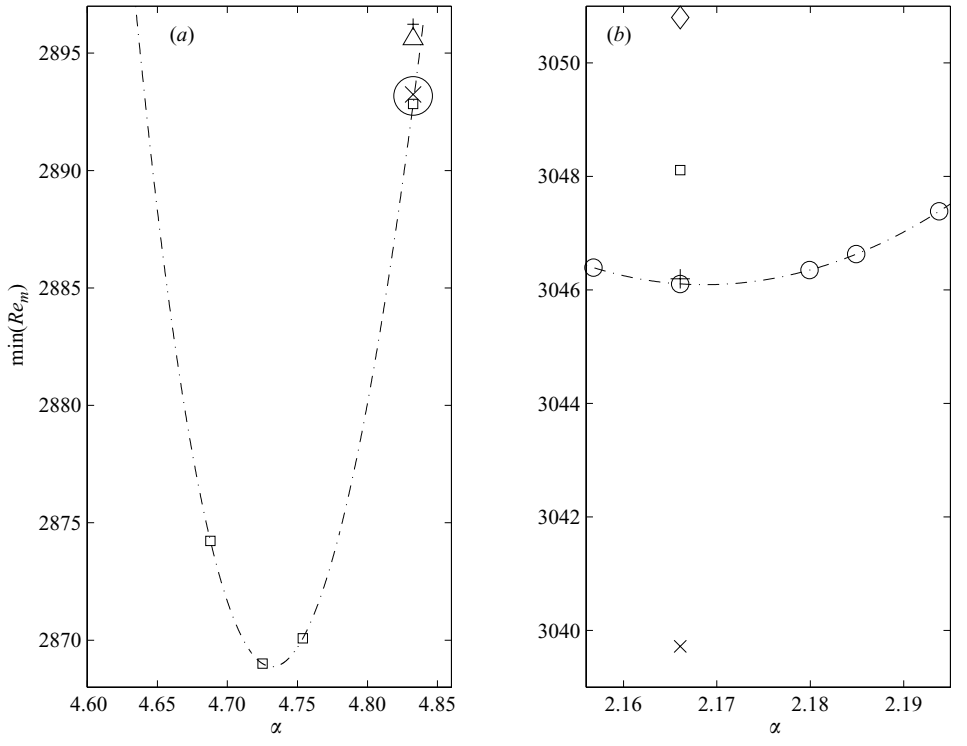

FIGURE 27. Dependence of the critical mean Reynolds number Re_m on the streamwise wavenumber α. (*a*) $\mathscr{R}_6$ travelling waves with truncations (M, N, L): □ (7, 40, 5) (with polynomial fit), △ (7, 40, 4), × (7, 40, 6), ○ (8, 40, 5), + (7, 45, 4). These indicate that the truncation (7, 40, 5) is high enough to estimate the minimum to ± 2 accuracy. (*b*) The subharmonic $\mathscr{R}_1$ travelling waves and truncations: ○ (9, 35, 5) (with polynomial fit), + (9, 36, 5), □ (9, 34, 5), × (9, 32, 5) and ◇ (8, 35, 5).

$Re < 6000$ is an extreme example of this.) Whereas for increasing m_0, the rolls interact less but get closer to the wall and become more damped. As a result, the threshold Reynolds number increases with m_0.

The new solutions have been found using a constructive and mechanistically motivated continuation procedure developed by Waleffe in the context of plane Couette and Poiseuille flow. This is based upon manufacturing a flow in which streamwise rolls, streaks and three-dimensional waves symbiotically sustain themselves against viscosity by drawing energy out of the mean flow. The fact that this technique has worked in pipe flow, the third and perhaps most famous canonical example of wall-bounded shear flow, vindicates the approach and confirms that the same generic physical mechanisms are at play.

In a sense the travelling wave solutions exhibited here merely scratch the surface of the set of all possible travelling wave solutions. Even within the specific symmetry groups considered here, there are potentially numerous other possibilities which could arise by allowing greater flexibility in the radial structure of the streamwise rolls and/or by selecting wavelike instabilities with different symmetries. Certainly in terms of the fundamental waves, we have opted for the simplest structure under the plausible assumption that these will appear first as the Reynolds number increases. Beyond the symmetries imposed here, more families of travelling waves exist which are symmetric with respect to $\mathscr{Z}$ rather than $\mathscr{S}_2$ (these are left for future work).

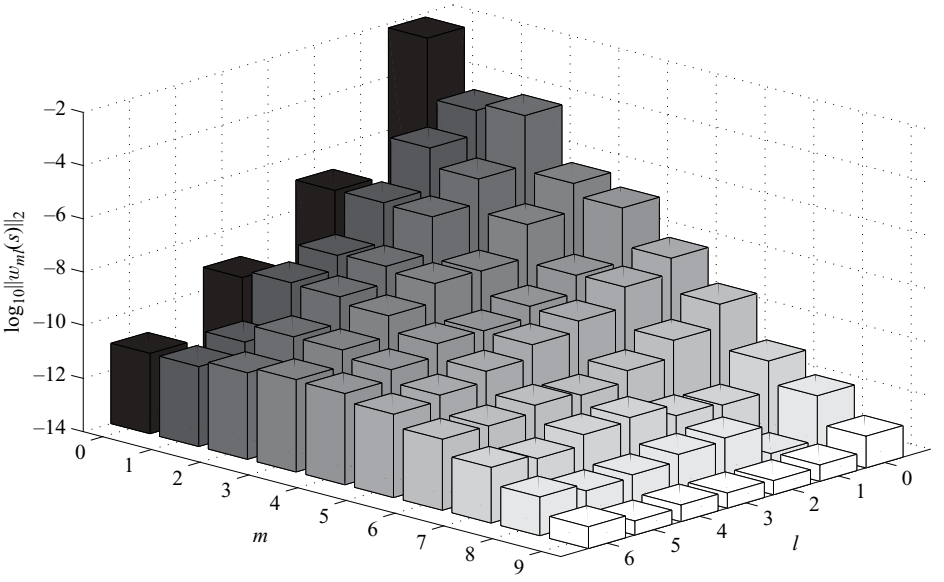

FIGURE 28. An example of the spectral energies ($\|w_{ml}(s)\|_2 := \sqrt{\int_0^1 s|w_{ml}|^2\,\mathrm{d}s}$) in the axial and azimuthal spectral representation of the axial velocity for the $\mathscr{R}_3$ travelling wave at its saddle-node bifurcation for $\alpha = 2.44$ (truncation (9, 35, 6).

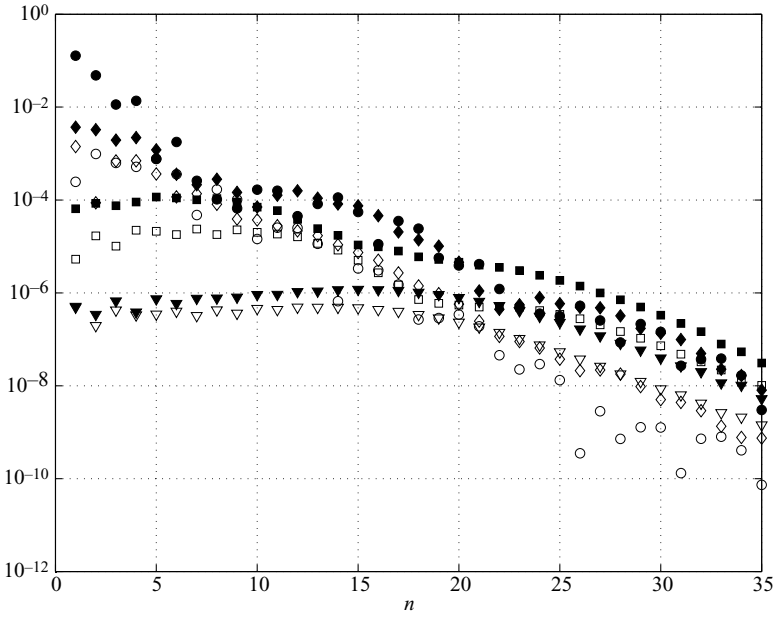

FIGURE 29. An example of the spectral energies in the radial spectral representation of the radial and axial velocities for the $\mathscr{R}_3$ travelling wave at its saddle-node bifurcation for $\alpha = 2.44$ (truncation (9, 35, 6)). The magnitudes of w_{n00} (solid circle), w_{n11} (solid diamond), w_{n33} (solid square), w_{n85} (solid triangle), u_{n11} (diamond), u_{n10} (circle), u_{n33} (square), u_{n85} (triangle) are plotted on a log scale against n, the radial spectral order.

Given that pipe flow can undergo transition at $Re_m \approx 1800$–2000, it is perhaps surprising that not more travelling waves have been found to exist below this value. This may motivate a greater search for other travelling waves or imply that even a small number of travelling waves are sufficient, through subsequent local and global bifurcations, to breed a phase space sufficiently complicated to rationalize the transitional dynamics seen. Certainly an immediate challenge is to try to identify the signatures of these travelling waves in both observational and numerical data with a view to understanding how their presence may contribute to the mean properties of transitional flows.

It's a pleasure to thank Fabian Waleffe for many helpful discussions during the course of this work and Bruno Eckhardt for sharing his preprint with us and making a number of constructive comments. R. R. K. is supported by EPSRC under grant GR/A92613/01 and H. W. by an EPSRC doctoral training grant.

REFERENCES

Anson, D. K., Mullin, T. & Cliffe, K. A. 1989 A numerical and experimental investigation of a new solution in the Taylor vortex problem. *J. Fluid Mech.* **207**, 475–489.

Barnes, D. R. & Kerswell, R. R. 2000 New results in rotating Hagen-Poiseuille flow. *J. Fluid Mech.* **417**, 103–126.

Benney, D. J. 1984 The evolution of disturbances in shear flows at high Reynolds numbers. *Stud. Appl. Maths* **70**, 1–19.

Bergström, L. 1993 Optimal growth of small disturbances in pipe Poiseuille flow. *Phys. Fluids* **5**, 2710–2720.

Boberg, L. & Brosa, U. 1988 Onset of turbulence in a pipe. *Z. Naturforsch* **43**, 697–726.

Bottin, S., Dauchet, O., Daviaud, F. & Manneville, P. 1998 Experimental evidence of streamwise vortices as finite amplitude solutions in transitional plane Couette flow. *Phys. Fluids* **10**, 2597–2607.

Carlson, D. R., Widnall, S. E. & Peeters, M. F. 1982 A flow-visualization study of transition in plane Poiseuille flow. *J. Fluid Mech.* **121**, 487–505.

Chapman, S. J. 2002 Subcritical transition in channel flows. *J. Fluid Mech.* **451**, 35–97.

Clever, R. M. & Busse, F. H. 1992 Three-dimensional convection in a horizontal fluid layer subjected to a constant shear. *J. Fluid Mech.* **234**, 511–527.

Clever, R. M. & Busse, F. H. 1997 Tertiary and quaternary solutions for plane Couette flow. *J. Fluid Mech.* **344**, 137–153.

Darbyshire, A. G. & Mullin, T. 1995 Transition to turbulence in constant-mass-flux pipe flow. *J. Fluid Mech.* **289**, 83–114.

Dauchot, O. & Daviaud, F. 1995 Finite amplitude perturbation and spots growth mechanism in plane Couette flow. *Phys. Fluids* **7**, 335–343.

Davey, A. & Nguyen, H. P. F. 1971 Finite-amplitude stability of pipe flow. *J. Fluid Mech.* **45**, 701–720.

Daviaud, F., Hegseth, J. & Bergé, P. 1992 Subcritical transition to turbulence in plane Couette flow. *Phys. Rev. Lett.* **69**, 2511–2514.

Davies, S. J. & White, C. M. 1928 An experimental study of the flow of water in pipes of rectangular section. *Proc. R. Soc. Lond.* A **119**, 92–107.

Draad, A. A., Kuiken, G. D. C. & Nieuwstadt, F. T. M 1998 Laminar-turbulent transition in pipe flow for Newtonian and non-Newtonian fluids. *J. Fluid Mech.* **377**, 267–312.

Eckhardt, B., Faisst, H., Schmiegel, A. & Schumacher, J. 2002 Turbulence transition in shear flows. *Advances in Turbulence IX: Proc. Ninth European Turbulence Conference, Barcelona* (ed. I. P. Castro, P. E. Hancock & T. G. Thomas) pp. 701–708. ISBN 84-95999-07-2.

Eliahou, S., Tumin, A. & Wygnanski, I. 1998 Laminar-turbulent transition in Poiseuille pipe flow subjected to periodic perturbation emanating from the wall. *J. Fluid Mech.* **361**, 333–349.

Faisst, H. & Eckhardt, B. 2000 Transition from the Couette-Taylor system to the plane Couette system. *Phys. Rev.* E **61**, 7227–7230.

Faisst, H. & Eckhardt, B. 2003 Travelling waves in pipe flow. *Phys. Rev. Lett.* **91**, art. 224502.

Garg, V. K. & Rouleau, W. T. 1972 Linear stability of pipe Poiseuille flow. *J. Fluid Mech.* **54**, 113–127.

Hamilton, J. M., Kim, J. & Waleffe, F. 1995 Regeneration mechanisms of near-wall turbulence structures. *J. Fluid Mech.* **287**, 317–348.

Han, G., Tumin, A. & Wygnanski, I. 2000 Laminar-turbulent transition in Poiseuille pipe flow subjected to periodic perturbation emanating from the wall. Part 2. Late stage of transition. *J. Fluid Mech.* **419**, 1–27.

Herron, I. H. 1991 Observations on the role of vorticity on the stability of wall bounded flows. *Stud. Appl. Maths* **85**, 269–286.

Hof, B., Juel, A. & Mullin, T. 2003 Scaling of the turbulence transition threshold in a pipe. *Phys. Rev. Lett.* **91**, art. 244502.

Joseph, D. D. & Carmi, S. 1969 Stability of Poiseuille flow in pipes, annuli and channels. *Q. Appl. Maths* **26**, 575–599.

Keefe, L., Moin, P. & Kim, J. 1992 The dimension of attractors underlying periodic turbulent Poiseuille flow. *J. Fluid Mech.* **242**, 1–29.

Kerswell, R. R. & Davey, A. 1996 On the linear instability of elliptic pipe flow. *J. Fluid Mech.* **316**, 307–324.

Landman, M. J. 1990*a* On the generation of helical waves in circular pipe flow. *Phys. Fluids* A **2**, 738–747.

Landman, M. J. 1990*b* Time-dependent helical waves in rotating pipe flow. *J. Fluid Mech.* **221**, 289–310.

Lessen, M., Sadler, G. S. & Liu, T.-Y. 1968 Stability of pipe Poiseuille flow. *Phys. Fluids* **11**, 1404–1409.

Lundbladh, A. & Johansson, A. V. 1991 Direct simulation of turbulent spots in plane Couette flow. *J. Fluid Mech.* **229**, 499–516.

Meseguer, A. & Trefethen, L. N. 2003 Linearized pipe flow to Reynolds number 10^7. *J. Comput. Phys.* **186**, 178–197.

Nagata, M. 1990 Three-dimensional finite-amplitude solutions in plane Couette flow: bifurcation from infinity. *J. Fluid Mech.* **217**, 519–527.

Nagata, M. 1997 Three-dimensional traveling-wave solutions in plane Couette flow. *Phys. Rev.* E **55**, 2023–2025.

Nagata, M. 1998 Tertiary solutions and their stability in rotating plane Couette flow. *J. Fluid Mech.* **358**, 357–378.

O'Sullivan, P. L. & Breuer, K. S. 1994 Transient growth in a circular pipe flow. II. Nonlinear development. *Phys. Fluids* **6**, 3652–3662.

Patera, A. T. & Orszag, S. A. 1981 Finite-amplitude stability of axisymmetric pipe flow. *J. Fluid Mech.* **112**, 467–474.

Reddy, S. C., Schmid, P. J., Baggett, J. S. & Henningson, D. S. 1998 On stability of streamwise streaks and transition thresholds in plane channel flows. *J. Fluid Mech.* **365**, 269–303.

Reynolds, O. 1883 An experimental investigation of the circumstances which determine whether the motion of water shall be direct or sinuous and of the law of resistance in parallel channels. *Phil. Trans. R. Soc. Lond.* **174**, 935–982.

Rheinboldt, W. C. & Burkardt, J. V. 1983*a* A locally parameterized continuation process. *ACM Trans. Math. Software* **9**, 215–235.

Rheinboldt, W. C. & Burkardt, J. V. 1983*b* ALGORITHM 596 A program for a locally parameterized continuation process. *ACM Trans. Math. Software* **9**, 236–241.

Romanov, V. A. 1973 Stability of plane-parallel Couette flow. *Functional Anal. Applics.* **7**, 137–146.

Rozhdestvensky, B. L. & Simakin, I. N. 1984 Secondary flows in a plane channel: their relationship and comparison with turbulent flows. *J. Fluid Mech.* **147**, 261–289.

Salwen, H., Cotten, F. W. & Grosch, C. E. 1980 Linear stability of Poiseuille flow in a circular pipe. *J. Fluid Mech.* **98**, 273–284.

Schlichting, H. 1968 *Boundary-Layer Theory*. McGraw-Hill.

Schmid, P. J. & Henningson, D. S. 1994 Optimal energy density growth in Hagen-Poiseuille flow. *J. Fluid Mech.* **277**, 197–225.

Schmiegel, A. & Eckhardt, B. 1997 Fractal stability border in plane Couette flow. *Phys. Rev. Lett.* **79**, 5250–5253.

Smith, F. T. & Bodonyi, R. J. 1982 Amplitude-dependent neutral modes in the Hagen-Poiseuille flow through a circular pipe. *Proc. R. Soc. Lond.* A **384**, 463–489.

Tillmark, N. & Alfredsson, P. H. 1992 Experiments on transition in plane Couette flow. *J. Fluid Mech.* **235**, 89–102.

Toplosky, N. & Akylas, T. R. 1988 Nonlinear spiral waves in rotating pipe flow. *J. Fluid Mech.* **190**, 39–54.

Waleffe, F. 1995*a* Hydrodynamic stability and turbulence: Beyond transients to a self-sustaining process. *Stud. Appl. Maths* **95**, 319–343.

Waleffe, F. 1995*b* Transition in shear flows: Nonlinear normality versus non-normal linearity. *Phys. Fluids* **7**, 3060–3066.

Waleffe, F. 1997 On a self-sustaining process in shear flows. *Phys. Fluids* **9**, 883–900.

Waleffe, F. 1998 Three-dimensional coherent states in plane shear flows. *Phys. Rev. Lett.* **81**, 4140–4143.

Waleffe, F. 2001 Exact coherent structures in channel flow. *J. Fluid Mech.* **435**, 93–102.

Waleffe, F. 2003 Homotopy of exact coherent structures in plane shear flows. *Phys. Fluids* **15**, 1517–1534.

Waleffe, F. & Kim, J. 1997 How streamwise rolls and streaks self-sustain in a shear flow. *Self-Sustaining Mechanisms of Wall Turbulence* (ed. R. L. Panton), pp. 385–422. Computational Mechanics, Southampton.

Waleffe, F. & Kim, J. 1998 How streamwise rolls and streaks self-sustain in a shear flow: Part 2. *AIAA Paper* 98-2997.

Walton, A. G. 2002 The temporal evolution of neutral modes in impulsively started flow through a circular pipe and their connection to the nonlinear stability of Hagen-Poiseuille flow. *J. Fluid Mech.* **457**, 339–376.

Wygnanski, I. J & Champagne, F. H. 1973 On transition in a pipe. Part 1. The origin of puffs and slugs and the flow in a turbulent slug. *J. Fluid Mech.* **59**, 281–351.

Wygnanski, I. J, Sokolov, M. & Friedman, D. 1975 On transition in a pipe. Part 2. The equilibrium puff. *J. Fluid Mech.* **69**, 283–304.

Zikanov, O. Y. 1996 On the instability of pipe Poiseuille flow. *Phys. Fluids* **8**, 2923–2932.